Journal of Aerosol Science 172 (2023) 106193

Contents lists available at ScienceDirect

Journal of Aerosol Science

journal homepage: www.elsevier.com/locate/jaerosci

Modelling the electrophoretically-enhanced in-flame deposition of carbon nanoparticles

A. Parisi [a], G. De Falco [a], M. Sirignano [a,*], P. Minutolo [b], M. Commodo [b], C. Carotenuto [c], F. Di Natale [a]

[a] Dipartimento di Ingegneria Chimica, dei Materiali e della Produzione Industriale, Università degli Studi di Napoli "Federico II", 80125, Napoli, Italy
[b] Istituto di Scienze e Tecnologie per l'Energia e la Mobilità Sostenibili, STEMS-CNR, 80125, Napoli, Italy
[c] Dipartimento di Ingegneria, Università della Campania "L. Vanvitelli", 81031, Aversa (CE), Italy

A B S T R A C T

Flame synthesis of Carbon NanoParticle (CNP) films is gaining strong interest for novel industrial applications because of the easy tuning of the operating conditions that enables accurate control of the chemical and physical properties of the produced CNPs. This work proposes a novelty in the synthesis of CNP films, namely the possibility of applying electric fields in flame to trigger electrophoretic deposition phenomena. In this way, it is possible to add another degree of freedom to the harvesting process and potentially modify the properties of the CNP films, without changing the operating flame conditions. To investigate the physical mechanisms governing the thermo-electrophoretic deposition of CNPs, a numerical model to simulate the particle dynamics close to the collecting substrate has been developed, and experiments have been carried out to provide highly controlled test conditions that can be used to support model validation. The experimental results consist of Atomic Force Microscopy (AFM) measurements to determine the number of particles deposited after a controlled harvesting condition as a function of the applied electrophoretic force, imposed on the substrate by means of a DC voltage varied from 0 to -3kV. The AFM shows that the amount of deposited material increases up to six times when passing from an uncharged to the -3kV charged case. The model predictions are highly consistent with the AFM measurements and pointed out that the electric field in flame significantly alters the CNP deposition velocities and impact angles, which are likely to affect the properties of the film.

1. Introduction

Combustion-generated particles have been extensively associated with adverse health and environmental effects (Bernasconi et al., 2022; De Falco et al., 2017a; Magnani et al., 2016; Thompson, 2018; Wang et al., 2023). Hence, over the last decades, combustion-generated Carbon NanoParticles (CNPs) (Michelsen, 2017; Michelsen et al., 2020; Martin et al., 2022; Bauer et al., 2022; D'Anna, 2009) have received increasing attention driven by the need to reduce the emission factors of combustion processes and the evolution of scientific knowledge and technological capabilities in the fields of combustion, environmental science, and toxicology.

On the other hand, CNP-based materials are gaining increasing interest in material science, due to their high specific surface area (Chen & Dai, 2013; Zhang et al., 2010a), biocompatibility (Kümmerer et al., 2011; Souza & Fernando, 2016), superhydrophobicity (Khan et al., 2021; Seo et al., 2014) as well as fascinating optical and electrical properties (De Falco et al., 2014; De Falco et al., 2017b, De Falco et al., 2021; Minutolo et al., 2022; Veronesi et al., 2022) that have encouraged their use in various fields such as bio-imaging (Bhunia et al., 2013; Boakye-Yiadom et al., 2019; Dinger et al., 2022; Molkenova et al., 2020; Ray et al., 2009), nanomedicine (Liu et al., 2011; Loh et al., 2018; Zhang et al., 2014), sensor technology and energy storage (Islam & Saikia, 2022; Miao et al., 2020; Saini

* Corresponding author.
E-mail address: mariano.sirignano@unina.it (M. Sirignano).

https://doi.org/10.1016/j.jaerosci.2023.106193
Received 31 January 2023; Received in revised form 16 April 2023; Accepted 19 April 2023
Available online 26 April 2023

et al., 2021; Xiao et al., 2021).

CNPs materials are produced by a variety of methods, such as wet-chemistry, arc discharge, low-current glow discharge and gas-phase processes (Alam et al., 2017; Andhika et al., 2020; Sano, 2004; Sobczyk & Jaworek, 2021; Zhang et al., 2010b). Among these latter, flame synthesis appears as a valid option since it is autothermic, operable as a one-step process, with lower cost compared to other routes, and scalable to the industrial level (Commodo et al., 2015; De Falco et al., 2019; Kammler et al., 2001; Kelesidis et al., 2017; Li et al., 2016; Nersisyan et al., 2017; Roth, 2007; Sirignano et al., 2020; Zheng, 2002). CNPs produced in flames can be collected by employing thermophoretic deposition, *i.e.,* inserting a cold substrate in the flame environment (Messerer et al., 2003; Zhao et al., 2008; Zheng, 2002). Large temperature gradients, up to about 10^6 K/m, appear very close to the substrate, driving particles toward the surface thanks to the unbalanced Brownian diffusion phenomena known as thermophoresis. The formation of CNP thin films with different properties can be obtained by tuning combustion parameters and the substrate temperature (Commodo et al., 2015; De Falco et al., 2017b, De Falco et al., 2019; Kammler et al., 2001; Kelesidis et al., 2017; Kumar & Bhattacharya, 2012; Li et al., 2016; Nersisyan et al., 2017; Roth, 2007; Sirignano et al., 2020; Zheng, 2002).

De Falco et al. (De Falco et al., 2017b) have studied the morphological and electrical properties of flame-formed CNP thin films produced by thermophoretic harvesting in a laminar premixed ethylene-air flame at a fixed equivalence C/O ratio, deposition time, and height above the burner, HAB. A cold substrate is repeatedly inserted into the flame with controlled insertion and cooling-down times. The experiments revealed that the film properties change with the HAB and the C/O ratio and that it is possible to fine-tune the film thickness by opportunely combining the number of substrate insertions in flame and their duration. However, a low harvesting rate has been achieved at a low C/O ratio, due to the low amount of CNPs in flame and to the intrinsic low thermophoretic deposition rate. This implies long production times and, consequently, a less efficient and scalable process. Besides, the thermophoretic deposition provides film structures with low density and the film mechanical resistance is thus scarce (De Falco et al., 2017b; De Falco, Mattiello, et al., 2021; De Falco, Carbone, 2021).

Electrophoretic forces can be used to enhance the deposition rate (Boccaccini et al., 2006; Cohen et al., 2020; Diba et al., 2016; Ho et al., 2019; Jaworek et al., 2017; Kumar & Bhattacharya, 2012; Sardari et al., 2018; Sung et al., 2020; Wang et al., 2010; Zhitomirsky, 2006). The use of electric fields to trigger electrophoretic effects on CNP harvesting has been largely exploited in after-treatment equipment and high-precision measurements systems (Cid ÍUssembayev et al., 2021; Carotenuto et al., 2010; Di Natale et al., 2022) but less adopted for producing thin films, where a few examples on flame-generated titania and silica are reported (Sabzyan & Ghalami, 2019; Vemury et al., 1997; Xiong et al., 2017).

To ignite electrophoretic deposition, an electric field must be applied to the flame. Typically, this is achieved by applying an electric potential to the stabilization plate or the collector substrate. This has several effects on particle deposition and even on flame characteristics.

The extensive knowledge of electrostatic particle capture suggests that the presence of an electric field in flame enhances deposition efficiency (Sardari et al., 2018). In fuel-rich flame conditions, a relevant fraction of the produced CNPs acquires an electric charge mainly due to thermal ionization and diffusion charging phenomena (Maricq, 2004; Sgro et al., 2010, 2011). The charge fraction distribution of CNPs formed in flames has symmetric polarities and is in good agreement with Boltzmann's theory.

In electric-field- enhanced flame synthesis, it was also observed that the electric fields have a noticeable effect on primary CNPs size, agglomerate size, and probably their crystallinity, depending on the potential polarity at the substrate electrode when the burner is grounded (Kammler et al., 2003; Tolmachoff et al., 2009; Wang et al., 2010; Xiong et al., 2017; Zhao et al., 2008). This is due to the alteration of CNP residence time in flame depending on the polarity of the substrate: application of a potential with a given polarity accelerates the capture of CNPs with opposite polarity, reducing their residence time, while the opposite occurs for CNPs with the same polarity of the applied potential (Wang et al., 2010). Since CNP charge distribution is symmetric (Sgro et al., 2010, 2011), in principle symmetric deposition rate can be expected regardless of the applied potential. Nevertheless, the effects of electric fields on the flame hydrodynamics and the ions dynamics alter this simple behaviour.

It has long been common knowledge that an external electric field has dramatic visible effects upon a flame since this is essentially a thermal plasma system: flame distortion, flame extinction, and soot suppression have been evidenced since decennia (Altendorfner et al., 2011; Volkov et al., 2009; Zigan, 2018). These phenomena are due to mechanical forces acting on the molecules as a consequence of the ionic wind, which sensibly affects the physical parameters of the flame. Flames contain large amounts of ions and free electrons deriving from the thermal energy and the chemical reactions developing within them and it is usually recognised as plasma (Bradley & Ibrah1m, 1974; Butler & Hayhurst, 1998). The ionic wind theory claims that naturally occurring ions and electrons are accelerated in a flame in response to a Lorentz force from an external electric field generated between a grounded burner and its stabilizing plate. The charged species are extracted from the flame and undergo continuous non-reacting molecular collisions with neutral gaseous molecules thereby producing a net acceleration in the exhaust gas (Kuhl et al., 2017; Park et al., 2017).

Wang et al. (Wang et al., 2010) have studied the effect of a uniform electric field in a laminar premixed ethylene/air flame from a McKenna burner, where the burner was electrically grounded, whereas either positive or negative voltages were applied to the stabilization plate. They have shown that above a critical value for the electric field, the flame becomes unstable, firstly exhibiting flickering and then showing the onset of electric discharges. In particular, the electric breakdown potential under a negative field is about two times greater than that observed for a positive field and takes place well below the 3000 kV/m observed for dry air at ambient conditions (Biswas & Mitra, 1979).

Therefore, the motion of CNPs under the effects of an external electric field applied to a surface immersed in the flames is the result of the complex intertwining between electrostatic effects on the CNP charge, ionic wind effects and occurrence of the voltage leading to breakdown. Below the electric breakdown, only flame-generated ions are present. Positive ions are formed by cations, while the negative ones are mostly composed of electrons, whose mass is far lower than that of the cations. Therefore, the ionic wind mostly

follows the direction of the cation motion in the field. For a negative polarity applied to the substrate, flame cations and positive CNPs are attracted. The cations mass generates an appreciable ionic wind that further pushes the particles towards the substrate. For a positive polarity, negatively charged CNPs are attracted to the substrate, but repelled by the ionic wind.

Xiong et al. (Xiong et al., 2017) have studied the effects of a uniform external electric field and polarity on the production of titania-based films on a silicon substrate. Specifically, a stagnation-swirl-flame synthesis burner is used and a high-voltage power supply provides the voltage bias at its aluminium stabilizing plate, creating a uniform electric field between the grounded burner and the substrate. When the applied electric potential is below 400 V, oppositely charged particles have been attracted to the substrate, increasing their electrophoretic velocity but decreasing their in-flame growth and agglomeration, resulting in smaller particle sizes and more columnar-structured films with lower packing density. For voltages above 400 V, the authors argued that particles behave as they acquired the same charge polarity as the voltage bias applied, being repelled and residing in the flame longer, thus increasing in-flame agglomeration and particle size. This turned into a more branched-structured film growth with high packing density (Xiong et al., 2017).

As shown by Xiong et al. (Xiong et al., 2017) the acceleration, or the deceleration of CNPs toward the charged substrate, and the resulting alteration of their velocity and impact angle with the substrate is likely to be related to a modification of the achieved film morphology. Indeed, the growth of CNP films comprises several steps: CNP collision on the substrate (or on deposit), CNP adhesion to the clean substrate or CNPs deposit, and, finally, CNP deposit/film re-structuring (Kardar et al., 1986; Meakin et al., 1986; Rodríguez-Pérez et al., 2007; Tassopoulos & Rosner, 1989). The CNP motion above the deposit can be considered as the controlling mechanism for film growth assuming a complete passive deposit, for which CNP attachment and coagulation phenomena can be neglected (Rodríguez-Pérez et al., 2005, 2007).

The dynamics of CNPs close to the substrate depend on field forces (*e.g.* gravitational or electromagnetic fields), particle inertia, and Brownian diffusion, which give rise to a combination of deterministic motions and random motion trajectories (Kardar et al., 1986; Meakin et al., 1986; Rodríguez-Pérez et al., 2005, 2007; Tassopoulos & Rosner, 1989). The dimensionless Peclet number measures the relative importance of the deterministic CNPs motion to the Brownian random motion and it is defined as:

$$Pe_i = \frac{v_i d_{p,i}}{D_i} \tag{1}$$

Where v_i is the normal component of the particle arrival velocity and D_i is the CNP diffusion coefficient. In the limit case of $Pe \ll 1$, a purely diffusive CNPs deposit occurs and the generated film grows with a fractal structure predicted by the diffusion-limited aggregation model (Liu et al., 2017). On the other hand, for $Pe \gg 1$ there is a ballistic behaviour of the CNP and the deposits will be compact with a rough interface (Arai et al., 2022; Castillo et al., 2014; Conde et al., 2021; Zhao et al., 2015). The introduction of an electric field in the flame, and the onset of an electrophoretic deposition mechanism in combination with a pure thermophoretic one, may alter the particle velocity, and thus their characteristic Peclet number, giving rise to an alteration of the film properties. Unfortunately, an experimental determination of the CNPs trajectories and velocity close to the film substrate is not available.

This paper aims to contribute to the discussion by proposing new experiments and a mathematical model for the thermo-electrophoretic deposition of CNPs in flame. A mathematical model is used to describe the CNPs dynamics close to the collector surface and aims to understand how the application of an electric field over the collecting substrate alters the velocity and the trajectories of CNPs of different sizes and charges while they are in the flame. The experimental work is thought to support and validate the modelling data, a controlled flame reactor has been equipped with a CNP collector unit which is pneumatically driven to provide a single insertion of a substrate in the flame, at a given height above the burner (HAB), with controlled residence time and speed of insertion. CNPs deposited on substrates have been analysed by atomic force microscopy (AFM). The validated model could offer useful indications to predict the morphological characteristics of CNP films obtained in the same experimental conditions with a larger number of insertions in flame.

The experimental results allow us to shed light on the amount of CNPs deposited under the effects of thermophoretic and

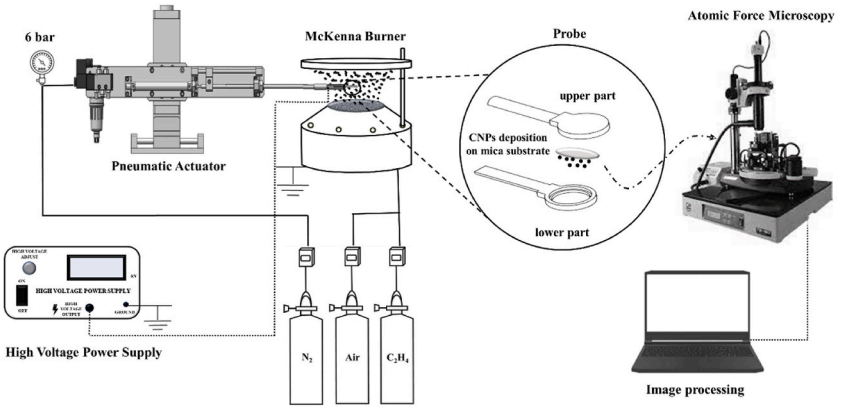

Fig. 1. Sketch of the electrophoretic deposition setup.

electrophoretic forces. The model results allow us to predict CNPs collisional probability with the substrate and to identify the main controlling mechanisms of the film formation process.

The paper is divided into three main sections: the description of i) the experimental setup and methodology and ii) the model equations to describe particle motion in the flame and their adhesion to the substrate and the characteristics of the numerical model used for their resolution and iii) the presentation of experimental and model results.

2. Experimental methods

A sketch of the thermos-electrophoretic deposition setup is shown in Fig. 1. This is an update of the thermophoretic deposition setup used by De Falco et al. (De Falco et al., 2014, 2021; De Falco et al., 2017b; Minutolo et al., 2022), with specific improvements aimed to allow stable and steady application of a DC electric potential on the surface of the collector.

A flat laminar premixed ethylene-air flame stabilized on a water-cooled McKenna burner was used as the CNPs-producing reactor. The carbon-to-oxygen ratio (C/O) was set to 0.67 with an air (N5.0 with 99.999% purity provided by Sol Group) flow rate of 13.06 L/min and an ethylene (N3.5 with 99.97% purity provided by Sol Group) flow rate of 1.79 L/min. Under these slightly sooting flame conditions, the cold gas velocity at the burner inlet is equal to 9.8 cm/s. This flame has been extensively characterized (Commodo et al., 2015, 2018; De Falco et al., 2014, 2017; De Falco et al., 2017b), showing that CNPs harvested at a *HAB* higher than 10 mm have a typical bimodal number particle size distribution (PSD), with a first mode around 2–3 nm and a second one made by particles larger than 10 nm. However, CNPs of the first mode give a negligible contribution in terms of relative mass to the total population, whereas most of the mass of the total population is due to CNPs of the second mode. Moreover, CNP charge distributions are also known from previous works (Sgro et al., 2010, 2011). The experiments indicate an equal distribution of positively and negatively charged particles sampled from flames at atmospheric pressure and that all the particles with sizes up to 20 nm carry on at most a single electric charge (Maricq, 2004, 2006). The PSD in number and the fraction of charged particles for the experimental condition investigated therein are shown in the following Fig. 8B.

CNPs were deposited on a freshly cleaved mica disk (d = 10 mm) substrate after a single rapid insertion in the flame by means of a homemade pneumatic actuator. The insertion time t_{ins} was 100 ms, and the *HAB* was 15 mm. It is worth mentioning that the insertion time has been optimized in order to minimize the overlapping effect and to collect an almost single layer of CNPs, keeping the degree of coverage as low as possible. The aluminium probe containing the substrate was kept at a fixed electric potential, while the burner and its stabilizing plate were grounded. Due to the small mica thickness (about microns), the electric potential on the mica substrate was considered exactly the same as that applied to the probe, even though mica is a dielectric material. This hypothesis was also verified by numerical simulations.

The electric potential on the substrate varied from 0 kV up to -3kV, below the onset of corona discharge, which appears at about −4 kV. In this work, only negative electric potentials were tested, since in presence of positive polarities, instabilities and flame extinctions have been observed, leading to a more complex interpretation of the experimental and model results.

Experimental setup conditions are summarized in Table 1.

AFM images of particles deposited on freshly cleaved mica substrates were acquired to estimate the degree of coverage (*i.e.* the area of CNP deposits per unit area of mica substrate) and to obtain a morphological characterization of CNPs deposits as a function of the applied potential. AFM measurements were performed with a Scanning Probe Microscope NTEGRA Prima from NT-MDT, operated in semi-contact mode in air and equipped with NANOSENSORS SSS-NCHR super-sharp silicon probes with a nominal tip radius of 2 nm.

3. Model description

In this section, we report the equations used to simulate the dynamics of CNPs close to a cold substrate immersed in a flat laminar ethylene-air premixed flame.

The model simulates the exact geometrical characteristics of the McKenna burner flame space, with its stabilization plate and with the substrate steadily kept in position inside the flame, according to the experimental conditions. The mathematical domain is thus a cylindrical space between the burner exit and the stabilization plate where the substrate is immersed in. Due to the extremely fast chemical kinetics and specific harvesting conditions, we assumed that no active chemistry is involved. Accordingly, the flame is made up of air entering the burner. Temperature (1500 K) and uniform axial velocity (0.50 m/s) simulating flame-burnt gases have been

Table 1
Experimental setup conditions.

Description (units)	Value
C/O ratio (−)	0.67
Air flow rate (L/min)	13.06
Ethylene flow rate (L/min)	1.79
Cold gas velocity (cm/s)	9.8
Sampling position *HAB* (mm)	15
Insertion time t_{ins} (ms)	100
Applied voltage V_0 (kV)	0;-1;-2;-3
Substrate	Mica
Number of insertions N_{ins} (#)	1

assigned at the burner exit (Carbone et al., 2017). The substrate is kept at 350 K when the simulation starts. The substrate is kept at a fixed applied potential while the burner and the stabilization plate are grounded.

The particle deposition model includes the resolution of the mass, momentum and energy balance in the gas phase, the Maxwell and Gauss equations for the assessment of the electric field and the particle's momentum balance to determine particle tracing. Considerations to estimate particle rebounds and adhesion on the substrate surface have been included to allow a more appropriate comparison with the experimental results. All the equations reported in this section are in vectorial notation. Both vectors and tensors are always reported in bold.

The model adopts Navier-Stokes equations for the conservation of momentum and the continuity equation for incompressible flows, by neglecting the influence of the electric field on the stress tensor:

$$\rho_g(\boldsymbol{u}\cdot\nabla\boldsymbol{u}) = \nabla\cdot\left[-P\underline{\boldsymbol{I}} + \mu_g\left(\nabla\boldsymbol{u} + \nabla\boldsymbol{u}^T\right)\right] \tag{2}$$

$$\nabla\cdot\boldsymbol{u} = 0 \tag{3}$$

Where ρ_g is the gas density; $\boldsymbol{u}$ is the velocity vector; P is the pressure; $\underline{\boldsymbol{I}}$ is the identity tensor and μ_g is the gas viscosity; $\nabla\boldsymbol{u}$ and $\nabla\boldsymbol{u}^T$ are, respectively, the velocity gradient tensor and its transposed; $\nabla\cdot\boldsymbol{u}$ is the divergence of the velocity vector. No slip condition is assigned on the physical walls and a suppress backflow condition is imposed on the lateral surface of the domain. A uniform axial velocity simulating flame-burnt gases is assigned at the base of the cylinder in correspondence with the burner exit:

$$\boldsymbol{u}_{wall} = \boldsymbol{0} \tag{4}$$

$$\left[-P\underline{\boldsymbol{I}} + \mu_g\left(\nabla\boldsymbol{u} + \nabla\boldsymbol{u}^T\right)\right]\cdot\boldsymbol{n} = -p_{out}\cdot\boldsymbol{n}$$

$$|\boldsymbol{u}_{inlet}| = 50\ \ cm/s$$

Where $\boldsymbol{u}_{wall}$ is the gas velocity vector on the physical walls; $\boldsymbol{n}$ is the outward surface normal vector; p_{out} is the pressure outside the domain, set to prevent the fluid from entering back into the domain; $|\boldsymbol{u}_{inlet}|$ is the normal inflow inlet velocity, equal to 50 cm/s at the inlet temperature of 1500 K (9.8 cm/s at ambient temperature) as in the experiments (De Falco et al., 2017b).

The flame temperature is modelled by solving the enthalpy balance as a boundary value problem of the form:

$$\rho_g c_{p,g}\boldsymbol{u}\cdot\nabla T + \nabla(-k\nabla T + q_r) = Q_{gen} \tag{5}$$

Where $c_{p,g}$ is the gas specific heat capacity at constant pressure; ∇T is the temperature gradient; k is the thermal conductivity; q_r is the heat flux by radiation estimated from our previous knowledge of the particle emissivity values (De Falco et al., 2017b; Maquin et al., 2000); Q_{gen} contains heat sources other than viscous dissipation such as the thermal power generated by the highly exothermic incomplete combustion reactions occurring in the flame (Yang et al., 2021; D'Anna, 2008; Balthasar & Frenklach, 2005; D'Anna et al., 2001). Computations are preliminarily performed for the unperturbed flow in the absence of the probe and, subsequently, by introducing the probe in the flame at an imposed temperature of 350 K.

By neglecting magnetic field effects, the Maxwell and Gauss laws are solved to simulate the electric field along the flame, considering a ground boundary condition on both the burner and the stabilization plate, and a constant DC electric potential applied on the substrate, V_0:

$$-\nabla\cdot(\varepsilon_m\nabla V) = \rho_{sc} \tag{6}$$

$$V_p = V_b = 0$$

$$V_{sub} = V_0$$

where V_{sub} is the electric potential at the substrate; V_p and V_b are, respectively, the electric potential values at the burner and the stabilization plate; ρ_{sc} is the net space charge density -*i.e.,* the difference of positive and negative ions concentration in a flame (Calcote, 1957; Calcote & Pease, 1951; Guo et al., 2003). Electrons, with their small mass and high mobility, have a high diffusion rate out of the flame, resulting in a spatial distribution of charge in the flame. In order to adjust the electrons and ions fluxed in flame, there is a self-induced electric field through the flame that accelerates positive ions and decelerates electrons, making them diffuse out of the flame front at an equal rate. The intrinsic electric field in the flame is described in terms of net space charge density (Butterworth & Cha, 2021). This parameter is a function of both flame fluid dynamics and the local Carbon-to-Oxygen ratio. An average value of the flame space-charge density is retrieved from the pertinent literature (Calcote & Pease, 1951).

The motion of dispersed CNPs in the flame can be modelled by the Langevin equation (Kim & Zydney, 2004; Vishnyakov et al., 2014). For each CNPs size d_p and each value for the CNPs charge q, its translational motion under the assumption of spherical shape is modelled as:

$$m\frac{d\boldsymbol{U}}{dt} = \boldsymbol{F}_D + \boldsymbol{F}_G + \boldsymbol{F}_B + \boldsymbol{F}_T + \boldsymbol{F}_E + \mathbf{F}_{DEP} + \boldsymbol{F}_i \tag{7}$$

where m is the mass of a single CNP; $\boldsymbol{U}$ is the relative velocity – *i.e.,* the difference between the particle velocity and the gas (flame)

velocity at each point in the domain. $\boldsymbol{F}_D$ is the viscous drag on a spherical CNP:

$$\boldsymbol{F}_D = \frac{3\pi\mu_g d_p \boldsymbol{U}}{C_c} \tag{8}$$

where d_p is the CNP diameter, and C_c is the Cunningham correction factor.

Due to the size of CNPs considered therein, the particle's motion is also affected by Brownian diffusion. This is the irregular wiggling motion of a particle caused by random variations in the relentless bombardment of gas molecules against the CNPs. The amplitude of Brownian excitation can be modelled with the Gaussian-with noise fictitious force:

$$\boldsymbol{F}_B = \boldsymbol{\zeta}\sqrt{\frac{6\pi k_B T d_p}{\Delta t}} \tag{9}$$

where $\boldsymbol{\zeta}$ is a zero-mean, unit-variance independent Gaussian random number vector; k_B is the Boltzmann constant; T is the absolute temperature and Δt is the time-step for the integration of the equation of particle motion.

$\boldsymbol{F}_G$ is the gravity (and buoyancy) body force:

$$\boldsymbol{F}_G = \frac{\pi}{6} d_p^3 (\rho_p - \rho_g)\boldsymbol{g} \tag{10}$$

where ρ_g is the gas density; ρ_p is the CNPs density and $\boldsymbol{g}$ is the gravitational acceleration.

$\boldsymbol{F}_T$ is the thermophoretic force:

$$\boldsymbol{F}_T = -\frac{P\lambda d_p^2 \nabla T}{T} \tag{11}$$

valid on the free molecule regime (Knudsen number Kn»1) limit, where P is the pressure and λ is the fluid mean free path.

In the operating conditions, CNP deposition is driven mostly by thermophoresis and viscous drag, since inertia and body forces are negligible because of their small sizes (Bongiorno et al., 2006; Fuchs et al., 1989; Hinds, 1999; Hwang et al., 2020). This is in line with former studies on the Brownian deposition mechanism which showed that this phenomenon is relevant only when the CNPs are within 100 nm distance from the collecting surface (Wang et al., 2010).

$\boldsymbol{F}_i$ reported in Eq. (7) represent a sum of all contributions from interaction forces between pairs of particles, *i.e.* the attractive van der Waals sintering force and the electrostatic forces between charged CNPs, normal repulsive, dissipative and attractive contact forces (Endres et al., 2021; Qian et al., 2022). For diluted systems, where the interparticle distance is higher than 5 times the CNPs diameter, these interparticle forces could be neglected. Moreover, if CNPs have sizes higher than 20 nm, the assumption of a spherical shape is not acceptable. In fact, particles larger than 20 nm appear as aggregates, which are clusters of primary particles that are chemically bonded by sinter-bridges with dimensions typically between 200 and 300 nm. For aggregated and agglomerates, the additional torque balance is needed (Endres et al., 2021; Qian et al., 2022):

$$\boldsymbol{M} = I\frac{d\boldsymbol{\omega}}{dt} = \boldsymbol{M}_F + \boldsymbol{M}_i \tag{12}$$

Where I is the CNP moment of inertia, $\boldsymbol{\omega}$ is the CNP angular velocity, $\boldsymbol{M}$ is the net torque, $\boldsymbol{M}_F$ is the resulting momenta related to the external long-range field and $\boldsymbol{M}_i$ is the resulting torque acting between pair of CNPs, which can be expressed as:

$$\boldsymbol{M}_i = -\boldsymbol{F}_t \times \boldsymbol{R}_p - \boldsymbol{M}_r \tag{13}$$

Where $\boldsymbol{F}_t$ is the tangential component of the friction forces related to the CNP against the tangential component of the velocity; $\boldsymbol{R}_p$ is the radius vector for a CNP and $\boldsymbol{M}_r$ is the rolling friction force acting against the angular velocity $\boldsymbol{\omega}$ (Endres et al., 2021).

When an external electric field is applied, charged CNPs are affected by an electrostatic force $\boldsymbol{F}_E$ (Li & Ahmadi, 1992; Sardari et al., 2018) near the deposition surface, which is given by the following expression:

$$\boldsymbol{F}_E = q\boldsymbol{E} - \frac{q^2}{16\pi\varepsilon_m z^2}\boldsymbol{n} \tag{14}$$

where q is the total charge carried by a CNP; $\mathbf{E}$ is the electric field vector; $\mathbf{n}$ is the unit vector orthogonal to the burner exit; ε_m is the flame permittivity. On the right-hand side of Eq. (14), the first term, $q\boldsymbol{E}$, is the Coulomb force due to the imposed electric field, and the second term is the image force, corresponding to the force created by an image charge of $-q$ at position $-z$ from the surface. Under the effect of an external field, the Coulomb force is dominant, the image force being relevant only at short-range very near the surface (Endres et al., 2021; Li & Ahmadi, 1992).

When CNPs are placed in a non-uniform electric field, they will be polarized leading to the attraction of CNPs, which are dependent on the relative polarizability of the CNPs and the surrounding medium (Jones, 2003; Jungmann et al., 2022; Markx & Pethig, 1995; Pohl, 1951). According to Maxwell-Wagner-Sillars theory (McKenzie et al., 2014; Xia et al., 2017) such polarization occurs at the CNP medium interface on a microscopic scale, leading to the separation of charges. This gives rise to a motion of particles toward the electrode known as dielectrophoresis, DEP. The strength of the DEP force ($\boldsymbol{F}_{DEP}$) varies with the properties of these CNPs and the suspension media. The simplest theoretical model for DEP is that of a homogeneous spherical particle immersed in a dielectric medium

(Irimajiri et al., 1979), which can be calculated according to the Pohl model (Pohl, 1951) as follows:

$$\boldsymbol{F}_{DEP} = \frac{\pi}{4} d_p^3 \varepsilon_m \mathrm{Re}(f_{CM}) \nabla \boldsymbol{E}^2 \tag{15}$$

Where ε_m is the medium permittivity and $\mathrm{Re}(f_{CM})$ is the real part of the Clausius-Mossotti factor (f_{CM}) (Jones, 2003; Markx & Pethig, 1995), which is defined in terms of complex permittivity as follows:

$$f_{CM} = \frac{\varepsilon_p^* - \varepsilon_m^*}{\varepsilon_p^* + 2\varepsilon_m^*} \tag{16}$$

Where $\varepsilon_p{}^*$ and $\varepsilon_m{}^*$ are the complex permittivity of the CNP and the suspension medium respectively. The calculation of the complex permittivity for CNP and medium is given below (Jones, 2003; Kirby, 2010):

$$\varepsilon_p^* = \varepsilon_p - \boldsymbol{i}\left(\frac{\sigma_p}{\omega_e}\right) \tag{17}$$

$$\varepsilon_m^* = \varepsilon_m - \boldsymbol{i}\left(\frac{\sigma_m}{\omega_e}\right) \tag{18}$$

Where ε_p is the CNP permittivity; σ_p is the CNP electrical conductivity; σ_m is the medium electrical conductivity; ω_e is the angular frequency of the electric field. If the angular frequency of the electric field is equal to zero, *i.e.*, direct current electric field-the real part of the complex permittivity becomes (Kirby, 2010):

$$\mathrm{Re}(f_{CM}) = \frac{\sigma_p - \sigma_m}{\sigma_p + 2\sigma_m} \tag{19}$$

The Langevin equation can be used to determine particle trajectories inside the flame, as they enter the domain through a given injection plane. The model is also able to calculate the fraction of particles that collide with the substrate, *i.e.*, the collisional probability ξ_i of each particle size.

To compare model results and experiments, it is necessary to make a direct comparison of the model result with the data in terms of the degree of coverage obtained by AFM. To this aim, it is possible to estimate the area A_i occupied by a CNP of diameter d_{pi} on the mica substrate, if the collisional probability ξ_i of each particle size is known:

$$A_i = \gamma_i \xi_i N_{i0} \frac{\pi}{4} d_{pi}^2 \tag{20}$$

In which N_{i0} is the number concentration of CNPs in the sampling point of the flame, as defined by the experimental data, γ_i is the sticking coefficient of a particle of diameter d_{pi}. Some clarification is needed regarding this parameter. CNPs reach the charged surface with an impact velocity $\boldsymbol{v_i}$ that is obtained by solving Eq. (7). According to the specific characteristics of the impact dynamics, particles may either adhere or rebound after collision with the substrate. Typically, particle rebounding from a surface has been considered an unwanted phenomenon causing artifacts in inertial impactors and reduction of the effective deposited particles. This suggests the importance of studying particle-surface interaction phenomena. The interaction can be understood through four basic phenomena: adhesion, rebound, resuspension and charge transfer. An adhesion force arising from the molecular interaction of a particle and a surface affects the particle in the adhesion force field within a distance from the surface. The extension of the adhesion force field depends on the material roughness and objects involved but for flame-formed nanoparticles, it is in the order of a few atomic layers, typically near 0.4 nm (Kuuluvainen et al., 2013; Kweon et al., 2015; Takeuchi, 2006).

For uncharged CNPs, the van der Waals interactions represent the main contribution to adhesion (De Falco et al., 2015). These interactions can be modelled in terms of Lennard-Jones potentials and the framework of the gas kinetic theory. In particular, it is considered that for CNP sizes smaller than 10 nm, a sticking coefficient significantly lower than 1 is expected because thermal rebound effects are likely to prevail over adhesion mechanisms due to van der Waals forces (D'Alessio et al., 2005). On the contrary, soot particles with a diameter larger than 10 nm are expected to stick after collision (D'Alessio et al., 2005).

This discrepancy is likely to be neglected in presence of a voltage since the adhesion mechanism includes additional attractive electric interaction forces with a potential increase in the sticking coefficient up to 1 (D'Alessio et al., 2005). In this model, sticking coefficients for uncharged CNPs produced in a C/O = 0.67 flame reported in D'Alessio et al. (D'Alessio et al., 2005) are used for both charged and uncharged particles and whatever the applied potential is. The total degree of coverage φ is the ratio between the total area occupied by all the CNPs and the mica substrate area, A_s.

$$\varphi = \frac{\sum_i A_i}{A_s} \tag{21}$$

It is worth noting that the model does not account for overlapping between CNPs. Hence two CNPs impacting in the same point on the mica disk are at the moment considered twice for the coverage. The effect of this hypothesis are discussed hereafter in the model validation section.

4. Numerical methods

COMSOL Multiphysics® (Chaurasia, 2022) finite element solver package has been used to solve the mass, momentum, energy balances, electric field equations, and the particle tracing model, using specific integrated software libraries.

The flame environment is represented as a cylindrical three-dimensional domain (diameter 6 cm and height 22 mm, as the distance between the burner exit and the stabilizing plate), generated within the COMSOL software using the internal geometry and functionality tools. In particular, the bottom and top circular surfaces of the cylinder represent the burner exit (namely the flame inlet) and the stabilizing plate (namely the flame outlet) respectively, while the side surface of the cylinder represents the interface between the flame and the surrounding outside air.

An aluminium holder including the deposition substrate has been positioned at a distance from the burner exit equal to the height above the burner of the real system ($HAB = 15$ mm) so that the centre of the deposition substrate coincides with the centre of the flame itself. A 3D CAD file for the holder has been imported to obtain its correct sizes. The aluminium holder is available at 350 K. A preliminary time-dependent numerical simulation shows that during the insertion time, a heating of about 5 K takes place, so that the holder temperature still remains below its melting temperature.

For the substrate, a flat disk with a 10 mm diameter and 150-μm thickness has been considered. All the physical properties of the substrate have been set equal to those of mica muscovite.

The numerical simulations for the flame have been carried out by using COMSOL Computational Fluid Dynamics, Heat Transfer, and AC/DC three-dimensional solvers. The specific physics interfaces used are Heat transfer and Laminar Flow, both of which are coupled to the Multiphysics of Non-Isothermal Flow, and Electrostatics, considering stationary conditions.

In particular, Eqs. (2) and (3) have been solved under the hypothesis of incompressible laminar flow with a reference pressure level equal to 1 atm. The fluid viscosity has been set equal to that of air, whereas the density is a simulation result. A normal inflow velocity of 50 cm/s has been considered as a boundary condition at the burner exit for the inlet flame (this corresponds to the 9.8 cm/s cold-gas velocity – 25 °C – set for the experimental setup), whereas for the flame outlet an ambient reference absolute pressure equal to 0 Pa with a compensation of the hydrostatic pressure and suppression of the backflow has been considered. Regarding the lateral walls, however, the standard no-slip condition has been used.

Furthermore, Eq. (5) has been solved for the heat transfer in the flame. Here, a reference temperature equal to 293.15 K has been used, applying a consistent stabilization with streamline and crosswind diffusion. Both at the flame inlet and outlet a thermal insulation condition has been applied. Additionally, the temperature at the holder and substrate surface has been set equal to 350 K, and a volumetric heat source equal to $Q_{gen} = 40$ W has been set to simulate the heat generated by the exothermic incomplete combustion reactions occurring in the flame (Yang et al., 2021; D'Anna, 2008; Balthasar & Frenklach, 2005; D'anna et al., 2001). Moreover, heat flux is added to the whole domain to consider the radiative heat losses estimated from the emissivity values for CNPs generated in flame (De Falco et al., 2017; Maquin et al., 2000).

Regarding electrostatics physics, the reference default impedance value of 50 Ohm for the terminals connected to grounding has been selected. A ground condition has been defined for both the flame inlet and outlet, while for the lateral walls, a zero charge condition has been considered. A space charge volume density has been defined, as $4.61 \cdot 10^{-10}$ C/m^3 as obtained indirectly by current-voltage measurements in other works retrieved in literature (Calcote, 1957; Calcote & Pease, 1951; Guo et al., 2003). Finally, an adjustable electric potential condition (V_0) has been applied to the holder.

All these equations have been first discretized on the flame domain and then solved via the finite element method (FEM). The FEM technique discretized the domain into finite elements and the dependent variables have been solved at nodes connecting these elements. This is done by multiplying the governing equation by weighting functions and integrating them to obtain their weak form. The solution has been then approximated at the element level, and the entire problem can be solved by assembling the elemental equations. The main advantage of the finite element method is its capacity to treat boundary conditions on curved surfaces.

To obtain fluid temperature, velocity, pressure, electric potential, and electric field, a three-dimensional unstructured mesh with four-node tetrahedral elements has been adopted. In the region close to the holder and substrate wall, where the boundary layers develop, mesh refinement is used. The Multifrontal massively parallel sparse direct solver has been used for all the simulations, with

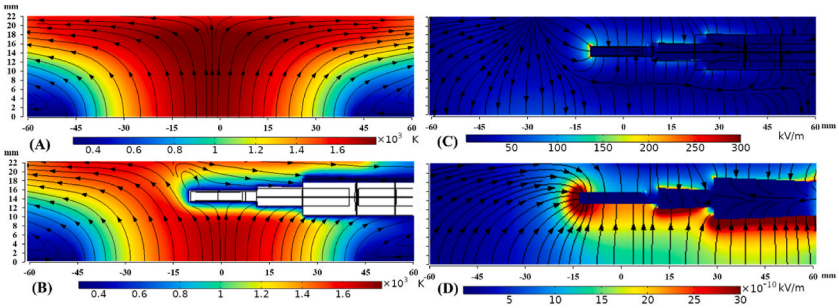

Fig. 2. Left: Temperature profile and velocity streamlines without (A) and with (B) the probe in flame; Right: Electric field intensity and lines (arrows) without (C) and with (D) the voltage applied to the probe. Images reported refer to the cut plane *rz* perpendicular to the burner plate, where *r* and *z* are the radial and axial coordinates.

the generalized minimum residual (GMRES) solver as a linear solver and the Newton iteration method as a nonlinear method. The relative tolerance has been set to 10^{-4}, but usually, values below 10^{-5} are reached.

Grid independence tests, from the numerical results, have been done with various grid sizes. From this process, a mesh with 807804 size elements and 39888 boundary elements has been built. This mesh is sufficient to achieve accuracy within 2% of that obtained by the maximum number of elements (820370 size elements and 43944 boundary elements).

Model results of temperature profiles and velocity streamlines with and without the probe inserted in flame and of the electric field modulus and streamlines without and with a voltage applied to the probe are reported in Fig. 2.

The comparison between the experimental axial temperature profiles reported in (Commodo et al., 2015) and the simulated one shows a very good agreement (*see* Fig. 3).

Even in the absence of an applied electric potential, the flame is characterized by an intrinsic (although very low) electric field, deriving from the imposed space-charge density. When potential is applied, a strong electric field perpendicular to the substrate establishes. The electric field has been simulated using the same mesh of the fluid dynamic field model.

CNPs are modelled with a discrete distribution, considering seven reference size bins at 2, 3, 5, 8, 10, 15 and 20 nm. The selected bins have been chosen to fully describe the experimental CNPs Size Distribution (PSD) (Commodo et al., 2013; Sirignano et al., 2017; Vitiello et al., 2019). The use of finer discretization does not affect the results. Modelled CNPs are considered single spheres, and this assumption is reasonable for the investigated size range (Endres et al., 2021; Qian et al., 2022). CNPs are released from the inlet burner boundary plane with a random spatial distribution at the bottom of the particle tracing domain. To allow a proper balancing between calculation time and significance of the model results, for particles up to 10 nm, $N_{in,i} = 5{\cdot}10^3$ particles have been injected in the particle tracing domain, while this number is doubled for the 15 and 20 nm particle size, to account for their lower thermophoretic deposition efficiency.

CNP motion has been modelled using Particle Tracing for the Fluid Flow interface with a one-way coupling approach: this implies that particle dynamics do not induce effects on the external fluid. When this physics interface is added, it is important to define particle properties in terms of density, diameter (d_p), charge number (Z) – the ratio between the CNP electric charge (q) and the elementary charge constant (e) – and type. CNPs have been approximated as solid spherical particles of density 1.8 g/mL (Alfà et al., 2007; Apicella et al., 2002), with variable diameters from 2 to 20 nm, and charge numbers (0, +1, or −1). It is important to underline that the spherical hypothesis is consistent with some experimental evidences for the selected size range (Endres et al., 2021; Morán et al., 2021). Particle release and propagation have been modelled using the Newtonian formulation with the Langevin correction (*see* Eq. (7)). In this module, it is possible to add some default forces, but also user-defined forces can be added. In particular, the gravity, the drag with the Cunningham-Millikan-Davies model, the Brownian, dielectrophoretic and the Coulomb electric forces have been selected from the default ones, since the COMSOL default equations are the same adopted in the model. Instead, thermophoretic and image forces have been user-defined (*see* Eq. (11) and the second addendum to the right of Eq. (14)).

It is worth pointing out that computational costs could be substantially reduced if negligible terms of Eq. (7) are not considered in the simulations. To this aim, an order of magnitude preliminary analysis of the relative importance of each force has been fulfilled and the results of this analysis for each CNP size are reported in Table 2, taking the magnitude of the viscous drag F_D as reference.

The order of magnitude analysis suggests that the gravity force can be neglected in simulations, since for all the CNP sizes its contribution is very small compared to the viscous drag. All the other forces should be taken into account since their relative importance varies with the CNP size.

To further balance the physical representativeness of the model results and computational costs, particle tracing has been calculated in a portion of the overall domain: the particle tracing domain is a cylindrical volume of a given diameter, which extends vertically from the burner to the substrate horizontal surfaces. The size of this cylinder is determined according to optimization and convergence criteria, as discussed in the following paragraph. Also in this domain, the calculations are performed using the same tetrahedral mesh of the overall computational domain. Fig. 4 shows the projection in the x-z plane of the domain for the flame

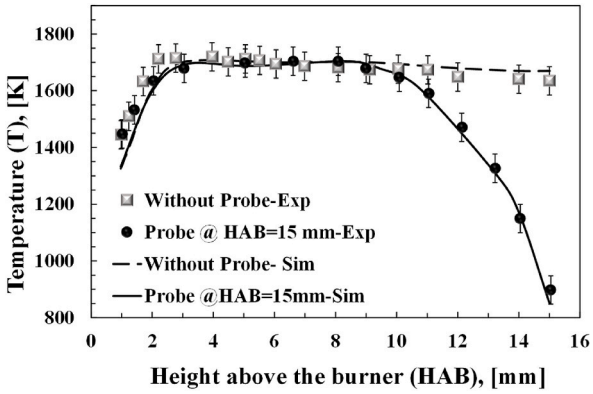

Fig. 3. Comparison between experimental (Commodo et al., 2015) and simulated temperature profile of the flame without and with the probe (HAB = 15 mm with C/O = 0.67). Experimental uncertainty: ±50 K. Simulation have been performed using a cylindrical dilution probe in order to accurately simulate the experimental apparatus used for the temperature profile measurements described in (Commodo et al., 2015).

Table 2
Order of magnitude analysis of the relative importance of each force (gravity $\mathbf{F}_G$, Brownian $\mathbf{F}_B$, thermophoresis $\mathbf{F}_T$, dielectrophoresis $\mathbf{F}_{DEP}$ and electric force $\mathbf{F}_E$) respect to the viscous drag $\mathbf{F}_D$ determined at 1 mm from the deposition substrate.

d_p, [nm]	F_G/F_D	F_B/F_D	F_T/F_D	F_{DEP}/F_D	F_E/F_D
s2	$9.0{\cdot}10^{-8}$	0.26	0.23	0.01	70
3	$1.0{\cdot}10^{-7}$	0.14	0.23	0.01	30
5	$2.0{\cdot}10^{-7}$	0.06	0.23	0.02	10
8	$3.0{\cdot}10^{-7}$	0.03	0.22	0.03	4
10	$4.0{\cdot}10^{-7}$	0.02	0.22	0.04	3
15	$6.0{\cdot}10^{-7}$	0.01	0.22	0.05	1
20	$8.0{\cdot}10^{-7}$	0.01	0.22	0.1	0.7

environment and the particle tracing with the adopted mesh. The mesh refinement area close to the substrate is also reported.

CNPs have been released from the inlet flame boundary plane with a random spatial distribution from the bottom of the particle tracing domain. At the lateral wall of this domain, a boundary condition of disappear has been set. Instead, a freeze condition has been set on the substrate to activate the Particle Counter node.

The diameter of the particle tracing domain has been determined from the numerical simulation. In particular, the minimum size of the cylindrical volume close to the deposition substrate was found as the one which guaranteed that all the positively charged CNPs were harvested when the maximum electric potential (*i.e.* −3 kV) was applied to the deposition substrate. Similarly, it was decided to optimise the release time of the CNPs in the control volume by defining a minimum duration that would not alter the results. CNPs injection in the volume could be better described as an instantaneous pulse – namely zero release time – or as a time-distributed injection – namely non-zero release time. For each domain size, the mesh is optimized to grand convergence of the results. The effects of the diameter of the particle tracing domain and the release time of collisional probability for positively charged particles of 10 nm are reported in Fig. 5 considering a standard COMSOL Fine mesh.

Fig. 5 shows that the duration of the release time does not affect the collisional probability, so this was minimized by assuming an instantaneous impulse. Moreover, the simulations indicate that the minimum particle tracing domain diameter is 10 mm, which is exactly the size of the deposition substrate. The computational time of the COMSOL model is greatly affected by the particle tracing step- Convergence for the steady state solution of the thermal-fluid dynamic and the electric fields requires 30 and 45 iterations respectively, while the particle tracing model requires 8000 iterations. The simulations results consist of profiles of velocity, temperature, pressure, electric potential, and electric field at each point of the domain and the different streamlines. Moreover, for CNPs it is possible to obtain information about the particle trajectories, the impact velocity vectors, and the number of particles that freeze on the substrate. Besides, the freezing position can be determined. From particle trajectory analysis, a collisional probability (ξ_b%)- the ratio between the number of harvested CNPs ($N_{out,i}$) and the number of injected ones ($N_{in,i}$)- can be determined. The fraction of covered area for each CNP size is calculated from Eq. (20) after fixing the sticking coefficient γ_i. Finally, the total degree of coverage φ is calculated with Eq. (21).

5. Experimental results

CNPs have been collected with a single insertion of 100 ms on mica disks varying the electric potential from 0 kV to -3kV. The insertion procedure was optimized to collect a significant number of particles whilst it is minimized the probability to deposit particles on already deposited particles so that the coverage area is representative of the particle capture rate. Fig. 6 shows AFM images for selected areas of the mica disk for different applied voltages. The images show that the number of deposited CNPs increases as the voltage increases. Using the Software Image J® to obtain image analysis it was verified the absence of columnar deposition of particles and the degree of coverage was found to increase by six times, from 5% at 0 kV to 30% at -3kV.

Interestingly, in the case of pure thermophoresis at 0 kV, CNPs are distributed uniformly on the substrate and appear mostly as single spherical entities or small aggregates of a few particles. This effect is consistent with former observations of the thermophoretic deposition mechanism (Buzio et al., 2000; De Falco et al., 2017b), according to which particles fall sequentially at apparently random points towards an initially flat surface and each particle sticks to the first point of contact. On the other hand, in presence of applied potential, CNPs are preferentially positioned close to another particle so that the deposit is organized as fractal petal-like structures. It

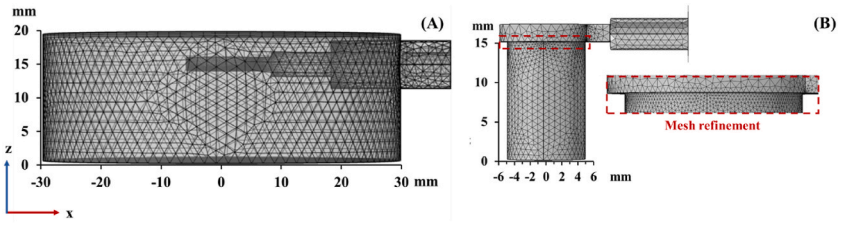

Fig. 4. **(A)** Geometry domain for the flame environment and **(B)** Particle tracing domain projected in the xz plane. The unstructured mesh with four-node tetrahedral elements and the mesh refinement adopted for the boundary layer are reported.

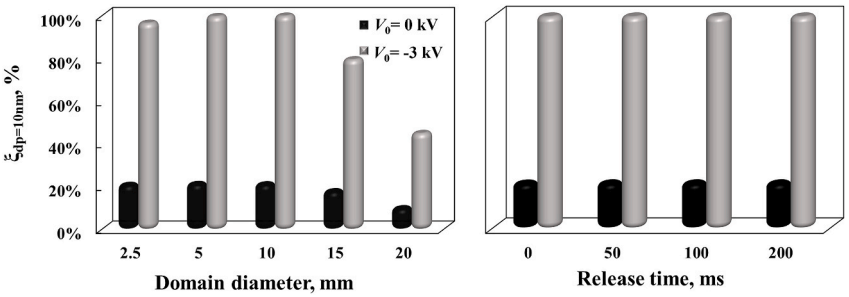

Fig. 5. Effects of the domain diameter (left) and release time (right) on the collisional probability (ξ, %) of 10 nm CNPs with a single positive charge in the absence ($V_0 = 0$ kV, black) and presence ($V_0 = -3$kV, grey) of an electric potential applied to the deposition substrate. A release time of 0 ms refers to an instantaneous pulse.

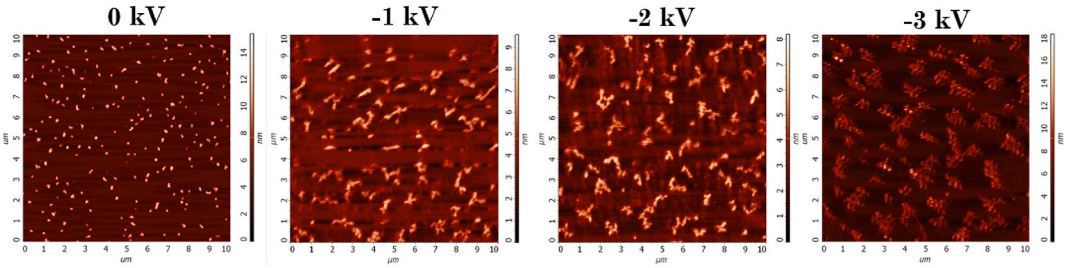

Fig. 6. AFM 2D images of the CNPs collected on a mica substrate with a single insertion of 100 ms in flame. (C/O = 0.67, HAB = 15 mm, t_{ins} = 100ms; N_{ins} = 1).

is beyond the scope and the limit of the proposed model to delve into details of the morphology of the deposits, that will be specific object of further investigation. However, literature studies suggest that the formation of the deposits can be described by using a diffusion-limited cluster aggregation (DLCA) model, according to which single CNPs deposited on the substrate after impacting on the surface, diffuse and aggregate to form larger fractal structures. Also polarization effects should be considered as well (Olevanov et al., 2004; Xiong et al., 2017): positively charged CNPs are deposited on the negatively charged substrate as a result of Coulomb interactions (Vishnyakov et al., 2014). CNPs reach the negative charge at equilibrium with the substrate. While other positively charged particles can be attracted by Coulomb interactions, the neutral CNPs in the flame – the majority – can be polarised by the applied field determining stronger adhesion over the already deposited particles due to the higher chemical affinity (Sgro et al., 2010, 2011). Indeed, CNPs fractal-like structures are also observed in other works for similar reasons (Liu et al., 1999; Nie et al., 2014).

6. Modelling results

To understand the controlling mechanism and the role of the electric field in the harvesting for each class of CNPs, simulations have

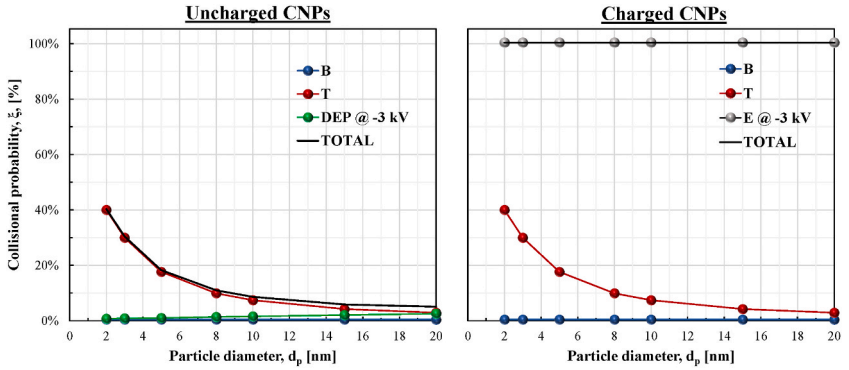

Fig. 7. Collisional probability of CNPs of different sizes for uncharged (left) and a single positive charge (right) CNPs. B: Brownian motion; T: Thermophoretic force; DEP: Dielectrophoretic force for uncharged CNPs with an applied voltage equal to −3 kV; E: Electrostatic force for charged CNPs with an applied voltage equal to −3 kV.

been conducted for different applied voltages, considering both uncharged and charged CNPs with and without the application of an electric field.

Fig. 7 shows the collisional probability related to Brownian, thermophoresis, Coulomb, and dielectric electrophoresis of uncharged and single (positive) charged CNPs over a substrate kept at – 3 kV, as a function of their size. These are obtained by applying the particle tracing model (Eq. (7)) with one single force plus the drag, $\boldsymbol{F}_D$, and interaction forces, $\boldsymbol{F}_i$, at a time.

Fig. 7 shows that for uncharged CNPs the resulting total collision probability (dark line) has a decreasing trend with CNPs sizes, passing from 40% to 1% for CNPs size increasing from 2 to 20 nm. Moreover, the contribution to the collisional probability due to the Brownian motion (B) is negligible for all CNPs classes. In the presence of an external electric field – when a voltage is applied to the deposition substrate – polarization phenomena are activated on the CNPs, determining the onset of dielectrophoretic force (DEP). This

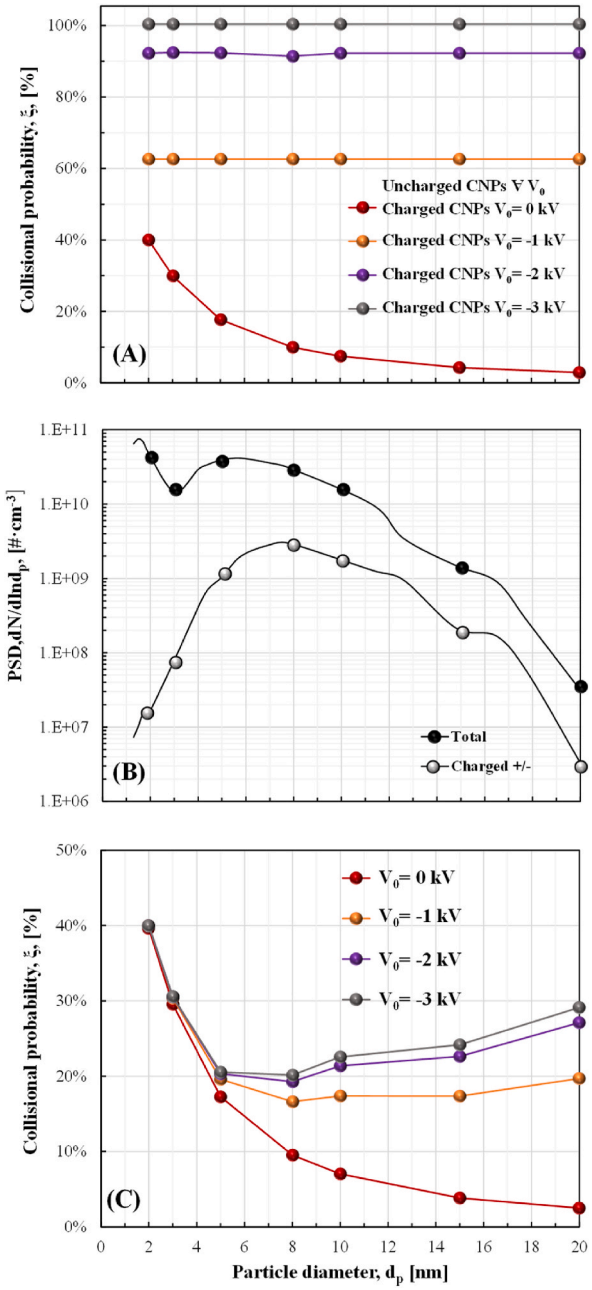

Fig. 8. (A): Total collisional probability for uncharged and for single charged CNPs varying the voltage applied to the deposition substrate from 0 kV to −3 kV. Note that for uncharged CNPs the collisional probability is always equal to that at 0 kV. **(B)**: Particle size distribution (PSD) in number for total (black) and single-charged CNPs (grey). **(C)**: Collisional probability (ξ,%) weighed against the size and charge distribution of CNPs adapted from (Sgro et al., 2010, 2011) as a function of the particle diameter varying the electric potential applied to the deposition substrate.

contribution becomes non-negligible only for CNPs larger than 5 nm, but it is still <4% of the total collisional probability. Indeed, for uncharged CNPs thermophoresis is the controlling mechanism for the harvesting, favouring the deposition of smaller CNPs, characterised by higher thermal mobility, and disfavouring the larger ones, whose inertia is higher and thermal mobility is lower. Thermophoresis favours the harvesting of smaller CNPs, both for the lower fraction of charged particles and for the higher thermal mobility. The fluid dynamic field and the Brownian motion allow small CNPs to randomly approach the substrate zone. At a distance <1 mm from the deposition substrate, due to the very high-temperature gradient (about 10^6 K/m) thermophoresis becomes larger than Brownian motion and CNPs motion becomes non-chaotic and directional.

For charged CNPs (Fig. 7, right), Brownian motion remains negligible and the effect of thermophoresis is similar to that obtained for uncharged CNPs. Ionic wind effects and dielectrophoretic forces have low effects on the deposition rate, but Coulomb electrophoresis provides a significant increase in the collisional probability, which reaches 100% for an applied potential of −3 kV. Moreover, the effect of the electric field is CNPs size-independent, being mostly influenced by the CNP charge (equal to a single cation in this calculation).

The results obtained for both charged and uncharged CNPs are consistent with the order of magnitude preliminary analysis shown in Table 2.

The calculated collisional probability can be applied to the actual particle size and charge distribution of flame CNPs at the sampling point, to compare with the experimental deposition data (C/O = 0.67, HAB = 15 mm).To this aim, Fig. 8 shows (from the top to the bottom) the total collisional probability values for uncharged CNPs and charged ones varying the voltages applied to the deposition substrate; the actual fraction of positively charged and uncharged CNPs and the resulting collisional probability values for CNPs weighed against the CNP size and charge distributions.

Fig. 8A reports the total collisional probability for each CNPs size on the deposition substrate as a function of the applied potential. As discussed in the comments of Fig. 7, for uncharged CNPs, thermophoresis is stronger than dielectrophoresis and ionic wind effects and therefore, the curve 0 kV refers to the harvesting of charged CNPs in absence of an external electric field but is also very close to that of uncharged CNPs for a charged substrate. For charged CNPs, there is an increase in the total collisional probability, which reaches 65% for an electric potential applied to the deposition substrate of −1 kV and up to 100% for an applied potential of −3 kV. Fig. 8B reports the PSD of CNPs used as input for this work together with the size distribution of single-charged (both positive and negative) CNPs achieved in the same experimental conditions tested in this work (Sgro et al., 2010, 2011). It is possible to see how below 8 nm the fraction of charged CNPs is less than 10% while reaching nearly 30% for CNPs larger than 10 nm. Modelling results on the collisional probability for each CNPs size as a function of the applied potential are reported in panel (C) of Fig. 8 taking into account the fraction of charged CNPs.

Fig. 8C shows that, due to the small fraction of CNPs smaller than 5 nm that is charged (Fig. 8B), the collisional probability for these particles is not affected by the applied electric field. On the other hand, thanks to the higher fraction of charged particles (Fig. 8B), a significant increase in the collision probability for CNPs larger than 5 nm appears after the application of the electric field. This increase is not linear: the collisional probability increases significantly in the transition from pure thermophoresis to an applied potential of −1 kV. For higher potentials, there is a weaker increase since mainly all particles are collected within the insertion time and saturation is reached for the system.

On the bases of the collisional probability data for the CNPs in the experimental flame conditions, and after the application of Eqs. (20) and (21), the surface coverage can be estimated. Fig. 9 resumes on the left the estimated degree of coverage as a function of the electric potential applied to the mica substrate and on the right the comparison between simulation and experimental values of the degree of coverage without and with the sticking coefficient correction.

From Fig. 9 it is possible to understand that there is a good agreement between the simulation and the experimental values for the degree of coverage, which goes from 5% to 30% passing from 0 to −3 kV. The increase in the degree of coverage is not linear, but it seems to reach an asymptotic value, also confirmed by the collisional probability values. Moreover, the sticking coefficient model of D'Alessio et al. (D'Alessio et al., 2005) valid for uncharged CNPs seems to be efficient in describing experimental results. It is worth noticing, indeed, that the sticking coefficient model can solve an error of estimation of the model which is exactly the same for

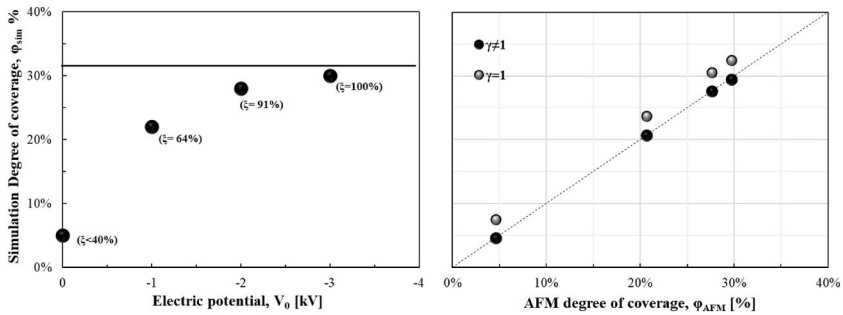

Fig. 9. Left: simulation results in terms of the degree of coverage as a function of the electric potential applied to the mica substrate. Values in brackets represent the corresponding values for the collisional probability if all the CNPs are positively charged. The horizontal line represents the degree of coverage if all the released CNPs were collected (complete harvesting). Right: Comparison between the simulation and the AFM degree of coverage without (grey) and with (black) the sticking coefficient correction. (C/O = 0.67, HAB = 15 mm, t_{ins} = 100ms; N_{ins} = 1).

thermophoretic and electrophoretic depositions, suggesting that particle rebounding is mostly related to the thermal agitation velocity of the CNPs rather than to the electrophoretic velocity.

It is worth to note that the degree of coverage, Eq. (21) is not the unique factor to characterize the particle capture rate as some particles attach on already deposited particles inducing no change on the degree of coverage. As previously observed, the fast single insertion procedure minimized the overlapping phenomenon. This is further confirmed by the agreement between the model and the experimental results. In general, there is a possibility that the degree of coverage underestimate particle capture rate. The presence of petal-like structure on the surface as evidenced by AFM images might suggest that this phenomenon is large and significant. However, these agglomerates are not present in the flame – as confirmed by 0 kV conditions and previous results – hence, they are likely to be formed during the deposition or on the surface of the substrate after the deposition due to their rearrangement, i.e., there is no effect of the particles themself in term of increasing particle capture rate.

Looking at overlapping, the simple presence of deposited particles on the surface can affect the estimation of particle capture rate by reducing the surface available for deposition, hence underestimate the degree of coverage. In this case the degree of coverage underestimation is proportional to the degree of coverage itself. It is worth to note that in this case for the investigated conditions this error would be no larger than 30% for the higher voltage and minimum for the no voltage conditions.

This latter consideration seem to be mitigated evaluating the height distribution of the deposited particles measured by the AFM. The deposition of an almost single layer of deposited CNPs over the substrate has been also verified for the electro/thermos phoretic deposition. Overall the petal-like structures are likely to be planar or only partially detached from the substrate. As stated above, a rearrangement of the structure on the surface during and/or after deposition could be responsible for this.

Finally, the model allows the estimation of particle velocity trajectories and modulus in the particle tracing domain, and, in particular, when they impact the substrate.

Table 3 summarises the mean and standard deviations of the velocity modulus and the impact angle distributions for the CNPs at 0 and -3 kV for 2, 5 and 10 nm particles.

The model results indicate that at 0 kV, the impacts of CNPs with the substrate is independent on their charge, since thermophoretic forces are dominant in both cases, as shown in Fig. 6. Instead, the charged CNPs impacts the substrate at a far larger velocity when the electric field is applied to the substrate. This is related to the component of velocity perpendicular to the substrate, while other components are scarcely affected by the potential. As a consequence, the impact angle becomes closer to the perpendicular, following the direction of the electric field, and the standard deviations of both the velocity and the angle are smaller. It is indeed relevant to notice that the impact velocity of uncharged particles is very similar for both charged and uncharged substrates. Therefore, following the indications of Castillo et al. (Castillo et al., 2014; Kardar et al., 1986; Meakin et al., 1986; Rodríguez-Pérez et al., 2005, 2007; Tassopoulos & Rosner, 1989), the model results indicate that uncharged particles are deposited according to a diffusional model, while for charged particles larger than 6 nm a ballistic deposition model is likely to take place. The role of this different impact velocity on the morphology of the CNPs films requires further investigations and will be the subject of following works.

7. Conclusions

CNPs harvesting and deposition on a substrate in flame with and without the presence of an electric field has been modelled by implementing all the force fields involved in the process in a commercial CFD software. The proposed model is able to identify the controlling mechanisms for the CNPs harvesting, as their size and charge vary.

For uncharged CNPs, or for an uncharged substrate, thermophoresis is the controlling mechanism of the harvesting process, theoretically favouring the deposition of smaller CNPs with higher thermal mobility. For uncharged CNPs, results are similar even in presence of an external electric field since polarization phenomena and dielectrophoretic forces are negligible. For charged CNPs, electrophoresis is the controlling mechanism for the harvesting process in presence of an external electric field with a resulting collisional probability that is size-independent.

Considering the PSD in the actual flame and the actual fractions of charged CNPs, Collisional probability is higher for small CNPs under pure thermophoretic conditions. However, the presence of resuspension and rebounding phenomena in particles smaller than 10 nm leads to a reduction in the actual number of particles adhering to the substrate. Furthermore, the presence of external electric fields determines a significant increase in the collisional probability for CNPs larger than 5 nm. A non-linear trend with the electric potential applied to the deposition substrate due to saturation phenomena is observed. The good agreement between modelling and AFM experimental results in terms of the degree of coverage provides a validation criterion for the model.

Model is also able to retrieve information on particle impact velocities. It suggests that electrophoretic harvesting implies higher impact velocities and more perpendicular impact angles, consequently, a partial transition from a diffusion-controlled to a ballistic deposition mechanism is expected. Further experimental and numerical investigations on this aspect can shed light on the nature of deposited films and their possible applications.

Declaration of competing interest

The authors declare the following financial interests/personal relationships which may be considered as potential competing interests: Francesco Di Natale reports financial support was provided by Government of Italy Ministry of Education University and Research. Claudia Carotenuto reports was provided by Government of Italy Ministry of Education University and Research. Patrizia Minutolo reports financial support was provided by Government of Italy Ministry of Education University and Research.

Table 3
Mean and standard deviation (St.dev.) of CNPs impact velocity and impact angle for the CNPs at 0 kV (either charged or uncharged) and the single-charged CNPs at −3 kV.

Parameter	Descriptor	$d_p = 2$ nm		$d_p = 5$ nm		$d_p = 10$ nm	
		0 kV $q = 0, +1e$	−3 kV $q = +1e$	0 kV $q = 0, +1e$	−3 kV $q = +1e$	0 kV $q = 0, +1e$	−3 kV $q = +1e$
Impact velocity	Mean, m/s	0.50	20.19	0.50	20.33	0.50	20.24
	St. dev., -	7.3%	2.1%	7.4%	1.7%	9.4%	1.4%
Impact angle	Mean, °	83.84	88.77	82.36	88.89	81.72	89.10
	St.dev., °	4.48	1.36	4.05	0.83	3.56	0.67
Peclet number	Mean, -	$3.45{\cdot}10^{-4}$	$1.41{\cdot}10^{-2}$	$5.53{\cdot}10^{-3}$	0.225	$4.51{\cdot}10^{-2}$	1.66
	St.dev., -	$4.98{\cdot}10^{-5}$	$1.86{\cdot}10^{-3}$	$8.16{\cdot}10^{-4}$	0.031	$5.18{\cdot}10^{-3}$	0.63

Data availability

Data will be made available on request.

Acknowledgements

This work was financially supported by the PRIN project 2017PJ5XXX: “MAGIC DUST”.

List of Symbols

A_i	Area occupied by a single CNP
A_s	Mica Substrate area
AFM	Atomic Force Microscopy
C_c	Cunningham correction factor
CNP	Carbon nanoparticle
C/O	Carbon to oxygen ratio
$c_{p,g}$	Gas specific heat capacity at constant pressure
D_i	CNP diffusion coefficient
d_p/d_{pi}	CNP diameter
$\boldsymbol{E}$	Electric field vector
e	Elementary electric charge
$\boldsymbol{F}_B$	Brownian excitation amplitude
$\boldsymbol{F}_D$	Friction force on a spherical CNP
$\boldsymbol{F}_{DEP}$	Dielectrophoretic force for uncharged CNP
$\boldsymbol{F}_E$	Electrostatic force for charged CNP
$\boldsymbol{F}_i$	Interaction forces
$\boldsymbol{F}_G$	Gravity and buoyancy body force
$\boldsymbol{F}_T$	Thermophoretic force
$\boldsymbol{F}_t$	Tangential component of the friction forces to the CNP against the tangential component of velocity
f_{CM}	Clausius-Mossotti factor
$\boldsymbol{g}$	Gravitational acceleration
HAB	Height above the burner
I	Moment of inertia
$\underline{\boldsymbol{I}}$	Identity tensor
k	Thermal conductivity
k_B	Boltzmann constant
$\boldsymbol{M}$	Net torque
m	Mass of a single CNP
$\boldsymbol{M}_F$	Resulting momenta related to the external long-range field
$\boldsymbol{M}_i$	Resulting torque acting between pair of CNPs
$\boldsymbol{M}_r$	Rolling friction force acting against the angular velocity
$N_{in,i}$	Number of injected CNPs
N_{i0}	Number of inlet CNPs in the real flame
N_{ins}	Number of insertions in flame
$N_{out,i}$	Number of harvested CNPs
$\boldsymbol{n}$	Outward surface normal unit vector
P	Pressure

Pe_i	Peclet dimensionless number of each CNP
p_{out}	Pressure outside the domain
PSD	Particles sized distribution
q	Total charged carried by a CNP
q_r	Heat flux by radiation
Q_{gen}	Heat sources other than viscous dissipation
$Re(f_{CM})$	Real part of the Clausius-Mossotti factor
$\boldsymbol{R}_p$	Radius vector
T	Absolute Temperature
t_{ins}	Insertion time-time for a single insertion
$\boldsymbol{U}$	Relative CNP velocity
$\boldsymbol{u}$	Flame velocity vector
$\boldsymbol{u}_{inlet}$	Normal inflow inlet velocity vector
$\boldsymbol{u}_{wall}$	Flame velocity vector on the physical walls of the domain
V	Electric potential
V_0	Electric potential applied to the deposition substrate
V_b	Electric potential at the burner exit
V_p	Electric potential at the stabilization plate
v_i	CNP impact velocity modulus
z	Distance from the deposition surface
Z	Charge number – ratio between the CNP electric charge and the elementary charge constant
Δt	Time-step for particle integration
γ	CNP sticking coefficient
φ_{AFM}	Experimental degree of coverage obtained by AFM
φ_{sim}	Simulation degree of coverage
ε_m	Medium (flame) permittivity
ε_p	CNP permittivity
ε^*_m	Complex permittivity for the flame
ε^*_p	Complex permittivity for CNP
λ	Fluid mean free path
∇	Nabla operator
∇T	Temperature gradient
$\nabla \boldsymbol{V}$	Electric potential gradient
$\nabla \boldsymbol{u}$	Velocity gradient tensor
$\nabla \boldsymbol{u}^T$	Transposed velocity gradient tensor
$\nabla \cdot \boldsymbol{u}$	Divergence of the velocity vector
ξ_i	Collisional probability
ρ_g	Gas mass density
ρ_{sc}	Net space charge density
σ_m	Flame electrical conductivity
σ_p	CNP electrical conductivity
ω	CNP Angular velocity
ω_e	Angular frequency of the electric filed
$\boldsymbol{\zeta}$	Zero-mean, unit-variance independent Gaussian random vector number

References

Alam, A., Wan, C., & McNally, T. (2017). Surface amination of carbon nanoparticles for modification of epoxy resins: Plasma-treatment vs. wet-chemistry approach. *European Polymer Journal, 87*, 422–448. https://doi.org/10.1016/j.eurpolymj.2016.10.004

Alfà, M., Apicella, B., Barbella, R., Tregrossi, A., & Ciajolo, A. (2007). Distribution of soot molecular weight/size along premixed flames as inferred by size exclusion chromatography. *Energy and Fuels, 21*, 136–140. https://doi.org/10.1021/ef060320p

Altendorfner, F., Kuhl, J., Zigan, L., & Leipertz, A. (2011). Study of the influence of electric fields on flames using planar LIF and PIV techniques. *Proceedings of the Combustion Institute, 33*, 3195–3201. https://doi.org/10.1016/j.proci.2010.05.112

Andhika, I. F., Saraswati, T. E., & Hastuti, S. (2020). The structural characteristics of carbon nanoparticles produced by arc discharge in toluene without added catalyst or gases. *Evergreen, 7*, 417–428. https://doi.org/10.5109/4068622

Apicella, B., Ciajolo, A., Suelves, I., Morgan, T. J., Herod, A. A., & Kandiyoti, R. (2002). Structural characterization of products from fuel-rich combustion: An approach based on size exclusion chromatography. *Combustion Science and Technology, 174*, 345–359. https://doi.org/10.1080/713712962

Arai, H., Asami, K., Ito, H., & Katayama, N. (2022). Effect of the settings of electrospray deposition method on the structure and performance of the fuel cell catalyst layer. *Current Applied Physics, 39*, 296–303. https://doi.org/10.1016/j.cap.2022.05.014

Balthasar, M., & Frenklach, M. (2005). Detailed kinetic modeling of soot aggregate formation in laminar premixed flames. *Combustion and Flame, 140*, 130–145. https://doi.org/10.1016/j.combustflame.2004.11.004

Bauer, F. J., Braeuer, P. A. B., Aßmann, S., Thiele, M. A., Huber, F. J. T., & Will, S. (2022). Characterisation of the transition type in optical band gap analysis of in-flame soot. *Combustion and Flame, 243*. https://doi.org/10.1016/j.combustflame.2022.111986

Bernasconi, S., Angelucci, A., & Aliverti, A. (2022). A scoping review on wearable devices for environmental monitoring and their application for health and wellness. *Sensors, 22*. https://doi.org/10.3390/s22165994

Bhunia, S. K., Saha, A., Maity, A. R., Ray, S. C., & Jana, N. R. (2013). Carbon nanoparticle-based fluorescent bioimaging probes. *Scientific Reports, 3*. https://doi.org/10.1038/srep01473

Biswas, J. C., & Mitra, V. (1979). High-frequency breakdown and paschen law. *Applied Physics, 19*, 377–381.

Boakye-Yiadom, K. O., Kesse, S., Opoku-Damoah, Y., Filli, M. S., Aquib, M., Joelle, M. M. B., et al. (2019). Carbon dots: Applications in bioimaging and theranostics. *International Journal of Pharmacy, 564*, 308–317. https://doi.org/10.1016/j.ijpharm.2019.04.055

Boccaccini, A. R., Cho, J., Roether, J. A., Thomas, B. J. C., Jane Minay, E., & Shaffer, M. S. P. (2006). Electrophoretic deposition of carbon nanotubes. *Carbon N Y, 44*, 3149–3160. https://doi.org/10.1016/j.carbon.2006.06.021

Bongiorno, G., Podestà, A., Ravagnan, L., Piseri, P., Milani, P., Lenardi, C., et al. (2006). Electronic properties and applications of cluster-assembled carbon films. *Journal of Materials Science: Materials in Electronics, 17*, 427–441. https://doi.org/10.1007/s10854-006-8089-4

Bradley, D., & Ibrah1m, M. A. (1974). The effects of electrical fields upon electron energy exchanges in flame gases. *Combustion and Flame*, 43–52.

Butler, C. J., & Hayhurst, A. N. (1998). Measurements of the concentrations of free hydrogen atoms in flames from observations of ions: Correlation of burning velocities with concentrations of free hydrogen atoms. *Combustion and Flame, 115*, 241–252.

Butterworth, T. D., & Cha, M. S. (2021). Electric field measurement in electric-field modified flames. In *Proceedings of the combustion institute* (Vol. 38, pp. 5347–5354). Elsevier Ltd. https://doi.org/10.1016/j.proci.2020.08.019.

Buzio, R., Gnecco, E., Boragno, C., Valbusa, U., Piseri, P., Barborini, E., et al. (2000). *Self-affine properties of cluster-assembled carbon thin films* (Vol. 444).

Calcote, H. F. (1957). Ion and electron profiles in flames. *Combustion and Flame, 9*.

Calcote, H. F., & Pease, R. N. (1951). Electrical properties of flames. Burner flames in longitudinal electric fields. *Industrial & Engineering Chemistry, 43*, 2726–2731.

Carbone, F., Gleason, K., & Gomez, A. (2017). Probing gas-to-particle transition in a moderately sooting atmospheric pressure ethylene/air laminar premixed flame. Part I: Gas phase and soot ensemble characterization. *Combustion and Flame, 181*, 315–328. https://doi.org/10.1016/j.combustflame.2017.01.029

Carotenuto, C., Di Natale, F., & Lancia, A. (2010). Wet electrostatic scrubbers for the abatement of submicronic particulate. *Chemical Engineering Journal, 165*, 35–45. https://doi.org/10.1016/j.cej.2010.08.049

Castillo, J. L., Martin, S., Rodriguez-Perez, D., Perea, A., & Garcia-Ybarra, P. L. (2014). Morphology and nanostructure of granular materials built from nanoparticles. *KONA Powder and Particle Journal, 31*, 214–233. https://doi.org/10.14356/kona.2014012

Chaurasia, A. S. (2022). *Computational fluid dynamics and comsol Multiphysics: A step-by-step approach for chemical engineers* (1st ed.). Palm Bay (USA): Apple Academy Press.

Chen, T., & Dai, L. (2013). Carbon nanomaterials for high-performance supercapacitors. *Materials Today, 16*, 272–280. https://doi.org/10.1016/j.mattod.2013.07.002

Cid Í, A., Ussembayev, Y. Y., Neyts, K., & Strubbe, F. (2021). Measurement of the amplitude and phase of the electrophoretic and electroosmotic mobility based on fast single-particle tracking. *Electrophoresis, 42*, 1623–1635. https://doi.org/10.1002/elps.202100030

Cohen, E., Lifshitz, M., Gladkikh, A., Kamir, Y., Ben-Barak, I., & Golodnitsky, D. (2020). Novel one-step electrophoretic deposition of the membrane-electrode assembly for flexible-battery applications. *J Mater Chem A Mater, 8*, 11391–11398. https://doi.org/10.1039/d0ta02328k

Commodo, M., De Falco, G., Bruno, A., Borriello, C., Minutolo, P., & D'Anna, A. (2015). Physicochemical evolution of nascent soot particles in a laminar premixed flame: From nucleation to early growth. *Combustion and Flame, 162*, 3854–3863. https://doi.org/10.1016/j.combustflame.2015.07.022

Commodo, M., De Falco, G., Minutolo, P., & D'Anna, A. (2018). Structure and size of soot nanoparticles in laminar premixed flames at different equivalence ratios. *Fuel, 216*, 456–462. https://doi.org/10.1016/j.fuel.2017.12.032

Commodo, M., Sgro, L. A., Minutolo, P., & D'Anna, A. (2013). Characterization of combustion-generated carbonaceous nanoparticles by size-dependent ultraviolet laser photoionization. *Journal of Physical Chemistry A, 117*, 3980–3989. https://doi.org/10.1021/jp401061d

Conde, J. J., Ferreira-Aparicio, P., & Chaparro, A. M. (2021). Electrospray deposition: A breakthrough technique for proton exchange membrane fuel cell catalyst layer fabrication. *ACS Applied Energy Materials, 4*, 7394–7404. https://doi.org/10.1021/acsaem.1c01445

D'Alessio, A., Barone, A. C., Cau, R., D'Anna, A., & Minutolo, P. (2005). Surface deposition and coagulation efficiency of combustion generated nanoparticles in the size range from 1 to 10 nm. In *Proceedings of the combustion institute* (Vol. 30, pp. 2595–2603). Elsevier Ltd. https://doi.org/10.1016/j.proci.2004.08.267.

D'Anna, A. (2008). Detailed kinetic modeling of particulate formation in rich premixed flames of ethylene. *Energy and Fuels, 22*, 1610–1619. https://doi.org/10.1021/ef700641u

D'Anna, A. (2009). Combustion-formed nanoparticles. *Proceedings of the Combustion Institute, 32 I*, 593–613. https://doi.org/10.1016/j.proci.2008.09.005

D'anna, A., Violi, A., D'Alessio, A., & Sarofim, A. F. (2001). A reaction pathway for nanoparticle formation in rich premixed flames. *Combustion and Flame, 127*, 1995–2003.

De Falco, G., Commodo, M., Bonavolontà, C., Pepe, G. P., Minutolo, P., & D'Anna, A. (2014). Optical and electrical characterization of carbon nanoparticles produced in laminar premixed flames. *Combustion and Flame, 161*, 3201–3210. https://doi.org/10.1016/j.combustflame.2014.05.021

De Falco, G., Commodo, M., D'Anna, A., & Minutolo, P. (2017). The evolution of soot particles in premixed and diffusion flames by thermophoretic particle densitometry. *Proceedings of the Combustion Institute, 36*, 763–770. https://doi.org/10.1016/j.proci.2016.07.108

Di Natale, F., Carotenuto, C., Parisi, A., Flagiello, D., & Lancia, A. (2022). Wet electrostatic scrubbing for flue gas treatment. *Fuel, 325*. https://doi.org/10.1016/j.fuel.2022.124888

Diba, M., Fam, D. W. H., Boccaccini, A. R., & Shaffer, M. S. P. (2016). Electrophoretic deposition of graphene-related materials: A review of the fundamentals. *Progress in Materials Science, 82*, 83–117. https://doi.org/10.1016/j.pmatsci.2016.03.002

Dinger, N., Panzetta, V., Russo, C., Netti, P. A., & Sirignano, M. (2022). In vitro effects of combustion generated carbon dots on cellular parameters in healthy and cancerous breast cells. *Nanotoxicology, 16*(6–8), 733–756. https://doi.org/10.1080/17435390.2022.2144775

Endres, S. C., Ciacchi, L. C., & Mädler, L. (2021). A review of contact force models between nanoparticles in agglomerates, aggregates, and films. *Journal of Aerosol Science*, 153. https://doi.org/10.1016/j.jaerosci.2020.105719

De Falco, G., Carbone, F., Commodo, M., Minutolo, P., & D'Anna, A. (2021). Exploring nanomechanical properties of soot particle layers by atomic force microscopy nanoindentation. *Applied Sciences, 11*. https://doi.org/10.3390/app11188448

De Falco, G., Commodo, M., Barra, M., Chiarella, F., D'Anna, A., Aloisio, A., et al. (2017b). Electrical characterization of flame-soot nanoparticle thin films. *Synthetic Metals, 229*, 89–99. https://doi.org/10.1016/j.synthmet.2017.05.008

De Falco, G., Commodo, M., Minutolo, P., & D'Anna, A. (2015). Flame-formed carbon nanoparticles: Morphology, interaction forces, and hamaker constant from AFM. *Aerosol Science and Technology, 49*, 281–289. https://doi.org/10.1080/02786826.2015.1022634

De Falco, G., Commodo, M., Minutolo, P., & D'Anna, A. (2019). Flame aerosol synthesis and thermophoretic deposition of superhydrophilic TiO2 nanoparticle coatings. *Chem Eng Trans, 73*, 37–42. https://doi.org/10.3303/CET1973007

De Falco, G., Mattiello, G., Commodo, M., Minutolo, P., Shi, X., D'Anna, A., et al. (2021). Electronic band gap of flame-formed carbon nanoparticles by scanning tunneling spectroscopy. In *Proceedings of the combustion institute* (Vol. 38)Elsevier Ltd. https://doi.org/10.1016/j.proci.2020.07.109, 1805–12.

De Falco, G., Terlizzi, M., Sirignano, M., Commodo, M., D'Anna, A., Aquino, R. P., et al. (2017a). Human peripheral blood mononuclear cells (PBMCs) from smokers release higher levels of IL-1-like cytokines after exposure to combustion-generated ultrafine particles. *Scientific Reports, 7*. https://doi.org/10.1038/srep43016

Fuchs, G., Treilleux, M., Santos Aires, F., Cabaud, B., Melinon, P., & Hoareau, A. (1989). Cluster-beam deposition for high-quality thin films. *Physical Review A- The Americal Physical Society, 40*, 6128–6130.

Guo, J., Goodings, J. M., Hayhurst, A. N., & Taylor, S. G. (2003). A simple method for measuring positive ion concentrations in flames and the calibration of a nebulizer/atomizer. *Combustion and Flame, 133*, 335–343. https://doi.org/10.1016/S0010-2180(03)00020-8

Hinds, W. (1999). Aerosol technology. Properties, behavior and measurement of airborne particles. Second Edi https://doi.org/10.1080/17449200600935521.

Ho, P. Y., Chen, C. K., & Huang, K. H. (2019). Combined effects of thermophoresis and electrophoresis on particle deposition in mixed convection flow onto a vertical wavy plate. *International Communications in Heat and Mass Transfer, 101*, 116–121. https://doi.org/10.1016/j.icheatmasstransfer.2018.12.019

Hwang, S. H., Okumura, T., Kamataki, K., Itagaki, N., Koga, K., & Shiratani, M. (2020). Size and flux of carbon nanoparticles synthesized by Ar+CH4 multi-hollow plasma chemical vapor deposition. *Diamond and Related Materials, 109*. https://doi.org/10.1016/j.diamond.2020.108050

Irimajiri, A., Hanai, T., & Inouye, A. (1979). A dielectric theory of "multi-stratified shell" model with its application to a lymphoma cell. *Journal of Theoretical Biology, 78*, 251–269.

Islam, N., & Saikia, B. K. (2022). An overview on atmospheric carbonaceous particulate matter into carbon nanomaterials: A new approach for air pollution mitigation. *Chemosphere, 303*. https://doi.org/10.1016/j.chemosphere.2022.135027

Jaworek, A., Sobczyk, A. T., Marchewicz, A., Krupa, A., Czech, T., Śliwiński, et al. (2017). Two-stage vs. two-field electrostatic precipitator. *Journal of Electrostatics, 90*, 106–112. https://doi.org/10.1016/j.elstat.2017.10.006

Jones, T. B. (2003). Basic theory of dielectrophoresis and electrorotation. *IEEE Engineering in Medicine and Biology Magazine, 22*, 33–42. https://doi.org/10.1109/MEMB.2003.1304999

Jungmann, F., Kruss, M., Teiser, J., & Wurm, G. (2022). Aggregation of sub-mm particles in strong electric fields under microgravity conditions. *Icarus, 373*. https://doi.org/10.1016/j.icarus.2021.114766

Kammler, H. K., Jossen, R., Morrison, P. W., Pratsinis, S. E., & Beaucage, G. (2003). The effect of external electric fields during flame synthesis of titania. *Powder Technology, 135–136*, 310–320. https://doi.org/10.1016/j.powtec.2003.08.023

Kammler, H. K., Mädler, L., & Pratsinis, S. E. (2001). Flame synthesis of nanoparticles. *Chemical Engineering & Technology, 24*, 583–596. https://doi.org/10.1002/1521-4125(200106)24:6<583::AID-CEAT583>3.0.CO;2-H

Kardar, M., Parisi, G., & Zhang, Y.-C. (1986). Dynamic scaling of growing interfaces. *Physical Reniew Letters, 56*, 889–892.

Kelesidis, G. A., Goudeli, E., & Pratsinis, S. E. (2017). Flame synthesis of functional nanostructured materials and devices: Surface growth and aggregation. *Proceedings of the Combustion Institute, 36*, 29–50. https://doi.org/10.1016/j.proci.2016.08.078

Khan, S. A., Ganeev, R. A., Boltaev, G. S., & Alnaser, A. S. (2021). Wettability modification of glass surfaces by deposition of carbon-based nanostructured films. *Fullerenes, Nanotubes, and Carbon Nanostructures, 29*, 576–587. https://doi.org/10.1080/1536383X.2021.1871897

Kim, M. M., & Zydney, A. L. (2004). Effect of electrostatic, hydrodynamic, and Brownian forces on particle trajectories and sieving in normal flow filtration. *Journal of Colloid and Interface Science, 269*, 425–431. https://doi.org/10.1016/j.jcis.2003.08.004

Kirby, B.(B. J.) (2010). *Micro- and nanoscale fluid mechanics : Transport in microfluidic devices*. Cambridge University Press.

Kuhl, J., Seeger, T., Zigan, L., Will, S., & Leipertz, A. (2017). On the effect of ionic wind on structure and temperature of laminar premixed flames influenced by electric fields. *Combustion and Flame, 176*, 391–399. https://doi.org/10.1016/j.combustflame.2016.10.026

Kumar, M., & Bhattacharya, S. (2012). Flame synthesis and characterization of nanocrystalline titania powders. *Processing and Application of Ceramics, 6*, 165–171. https://doi.org/10.2298/pac1203165k

Kümmerer, K., Menz, J., Schubert, T., & Thielemans, W. (2011). Biodegradability of organic nanoparticles in the aqueous environment. *Chemosphere, 82*, 1387–1392. https://doi.org/10.1016/j.chemosphere.2010.11.069

Kuuluvainen, H., Arffman, A., Saukko, E., Virtanen, A., & Keskinen, J. (2013). A new method for characterizing the bounce and charge transfer properties of nanoparticles. *Journal of Aerosol Science, 55*, 104–115. https://doi.org/10.1016/j.jaerosci.2012.08.007

Kweon, H., Yiacoumi, S., & Tsouris, C. (2015). The role of electrostatic charge in the adhesion of spherical particles onto planar surfaces in atmospheric systems. *Colloids and Surfaces A: Physicochemical and Engineering Aspects, 481*, 583–590. https://doi.org/10.1016/j.colsurfa.2015.06.030

Li, A., & Ahmadi, G. (1992). Dispersion and deposition of spherical particles from point sources in a turbulent channel flow. *Aerosol Science and Technology, 16*, 209–226. https://doi.org/10.1080/02786829208959550

Li, S., Ren, Y., Biswas, P., & Tse, S. D. (2016). Flame aerosol synthesis of nanostructured materials and functional devices: Processing, modeling, and diagnostics. *Progress in Energy and Combustion Science, 55*, 1–59. https://doi.org/10.1016/j.pecs.2016.04.002

Liu, Z., Robinson, J. T., Tabakmar, S. M., Yang, K., & Dai, H. (2011). Carbon materials for dryg delivery & cancer therapy. *Materials Today, 14*, 316–323.

Liu, B. G., Wu, J., Wang, E. G., & Zhang, Z. (1999). Two-dimensional pattern formation in surfactant-mediated epitaxial growth. *Physical Review Letters, 83*, 1195–1198. https://doi.org/10.1103/PhysRevLett.83.1195

Liu, D., Zhou, W., Qiu, Z., & Song, X. (2017). Fractal simulation of flocculation processes using a diffusion-limited aggregation model. *Fractal and Fractional, 1*, 1–14. https://doi.org/10.3390/fractalfract1010012

Loh, K. P., Ho, D., Chiu, G. N. C., Leong, D. T., Pastorin, G., & Chow, E. K. H. (2018). Clinical applications of carbon nanomaterials in diagnostics and therapy. *Advanced Materials, 30*. https://doi.org/10.1002/adma.201802368

Magnani, N. D., Muresan, X. M., Belmonte, G., Cervellati, F., Sticozzi, C., Pecorelli, A., et al. (2016). Skin damage mechanisms related to airborne particulate matter exposure. *Toxicological Sciences, 149*, 227–236. https://doi.org/10.1093/toxsci/kfv230

Maquin, B., Goyhénèche, J.-M., Goyhén, G., Goyhénèche, G., Derré, A., Derré, D., et al. (2000). Thermal conductivity of submicrometre particles: Carbon blacks and solid solutions containing C, B and N. *Journal of Physics D Applied Physics, 33*, 8–17.

Maricq, M. M. (2004). Size and charge of soot particles in rich premixed ethylene flames. *Combustion and Flame, 137*, 340–350. https://doi.org/10.1016/j.combustflame.2004.01.013

Maricq, M. M. (2006). A comparison of soot size and charge distributions from ethane, ethylene, acetylene, and benzene/ethylene premixed flames. *Combustion and Flame, 144*, 730–743. https://doi.org/10.1016/j.combustflame.2005.09.007

Markx, G. H., & Pethig, R. (1995). Dielectrophoretic separation of cells: Continuous separation. *Biotechnology and Bioengineering, 45*, 337–343. https://doi.org/10.1002/bit.260450408

Martin, J. W., Salamanca, M., & Kraft, M. (2022). Soot inception: Carbonaceous nanoparticle formation in flames: Soot inception. *Progress in Energy and Combustion Science, 88*. https://doi.org/10.1016/j.pecs.2021.100956

McKenzie, R., Zurawsky, W., & Mijovic, J. (2014). A molecular interpretation of Maxwell-Wagner-Sillars processes. *Journal of Non-Crystalline Solids, 406*, 11–21. https://doi.org/10.1016/j.jnoncrysol.2014.09.035

Meakin, P., Ramanlal, P., Sander, L. M., & Ball, R. C. (1986). A Ballistic deposition on surfaces. *Physical Review A, 34*, 5091–5103.

Messerer, A., Niessner, R., & Pöschl, U. (2003). Thermophoretic deposition of soot aerosol particles under experimental conditions relevant for modern diesel engine exhaust gas systems. *Journal of Aerosol Science, 34*, 1009–1021. https://doi.org/10.1016/S0021-8502(03)00081-8

Miao, L., Song, Z., Zhu, D., Li, L., Gan, L., & Liu, M. (2020). Recent advances in carbon-based supercapacitors. *Mater Adv, 1*, 945–966. https://doi.org/10.1039/d0ma00384k

Michelsen, H. A. (2017). Probing soot formation, chemical and physical evolution, and oxidation: A review of in situ diagnostic techniques and needs. *Proceedings of the Combustion Institute, 36*, 717–735. https://doi.org/10.1016/j.proci.2016.08.027

Michelsen, H. A., Colket, M. B., Bengtsson, P. E., D'Anna, A., Desgroux, P., Haynes, B. S., et al. (2020). A review of terminology used to describe soot formation and evolution under combustion and pyrolytic conditions. *ACS Nano, 14*, 12470–12490. https://doi.org/10.1021/acsnano.0c06226

Minutolo, P., Commodo, M., & D'Anna, A. (2022). Optical properties of incipient soot. *Proceedings of the Combustion Institute*. https://doi.org/10.1016/j.proci.2022.09.019

Molkenova, A., Toleshova, A., Song, S. J., Kang, M. S., Abduraimova, A., Han, D. W., et al. (2020). Rapid synthesis of nontoxic and photostable carbon nanoparticles for bioimaging applications. *Materials Letters, 261*. https://doi.org/10.1016/j.matlet.2019.127012

Morán, J., Henry, C., Poux, A., & Yon, J. (2021). Impact of the maturation process on soot particle aggregation kinetics and morphology. *Carbon N Y, 182*, 837–846. https://doi.org/10.1016/j.carbon.2021.06.085

Nersisyan, H. H., Lee, J. H., Ding, J. R., Kim, K. S., Manukyan, K.v., & Mukasyan, A. S. (2017). Combustion synthesis of zero-, one-, two- and three-dimensional nanostructures: Current trends and future perspectives. *Progress in Energy and Combustion Science, 63*, 79–118. https://doi.org/10.1016/j.pecs.2017.07.002

Nie, M., Mete, T., & Ellmer, K. (2014). Morphology and structure evolution of tin-doped indium oxide thin films deposited by radio-frequency magnetron sputtering: The role of the sputtering atmosphere. *Journal of Applied Physics, 115*. https://doi.org/10.1063/1.4871810

Olevanov, M. A., Mankelevich, Y. A., & Rakhimova, T. V. (2004). Coagulation and growth mechanisms for dust particles in a low-temperature plasma. *Journal of Experimental and Theoretical Physics, 98*, 287–304.

Park, D. G., Chung, S. H., & Cha, M. S. (2017). Visualization of ionic wind in laminar jet flames. *Combustion and Flame, 184*, 246–248. https://doi.org/10.1016/j.combustflame.2017.06.011

Pohl, H. A. (1951). The motion and precipitation of suspensoids in divergent electric fields. *Journal of Applied Physics, 22*, 869–871. https://doi.org/10.1063/1.1700065

Qian, W., Kronenburg, A., Hui, X., Lin, Y., & Karsch, M. (2022). Effects of agglomerate characteristics on their collision kernels in the free molecular regime. *Journal of Aerosol Science, 159*. https://doi.org/10.1016/j.jaerosci.2021.105868

Ray, S. C., Saha, A., Jana, N. R., & Sarkar, R. (2009). Fluorescent carbon nanoparticles: Synthesis, characterization, and bioimaging application. *Journal of Physical Chemistry C, 113*, 18546–18551. https://doi.org/10.1021/jp905912n

Rodríguez-Pérez, D., Castillo, J. L., & Antoranz, J. C. (2005). Relationship between particle deposit characteristics and the mechanism of particle arrival. *Physical Review E - Statistical, Nonlinear and Soft Matter Physics, 72*. https://doi.org/10.1103/PhysRevE.72.021403

Rodríguez-Pérez, D., Castillo, J. L., & Antoranz, J. C. (2007). Density scaling laws for the structure of granular deposits. *Physical Review E - Statistical, Nonlinear and Soft Matter Physics, 76*. https://doi.org/10.1103/PhysRevE.76.011407

Roth, P. (2007). Particle synthesis in flames. *Proceedings of the Combustion Institute, 31 II*, 1773–1788. https://doi.org/10.1016/j.proci.2006.08.118

Sabzyan, H., & Ghalami, F. (2019). Electric field effects on the growth of flame-synthesized nanosilica: A two-stage modeling. *Journal of the Iranian Chemical Society, 16*, 963–978. https://doi.org/10.1007/s13738-019-01591-9

Saini, D., Gunture, N., Kaushik, J., Aggarwal, R., Tripathi, K. M., & Sonkar, S. K. (2021). Carbon nanomaterials derived from black carbon soot: A review of materials and applications. *ACS Applied Nano Materials, 4*, 12825–12844. https://doi.org/10.1021/acsanm.1c02840

Sano, N. (2004). Formation of multi-shelled carbon nanoparticles by arc discharge in liquid benzene. *Materials Chemistry and Physics, 88*, 235–238. https://doi.org/10.1016/j.matchemphys.2004.07.018

Sardari, P. T., Rahimzadeh, H., Ahmadi, G., & Giddings, D. (2018). Nano-particle deposition in the presence of electric field. *Journal of Aerosol Science, 126*, 169–179. https://doi.org/10.1016/j.jaerosci.2018.09.012

Seo, K., Kim, M., & Kim, D. H. (2014). Candle-based process for creating a stable superhydrophobic surface. *Carbon N Y, 68*, 583–596. https://doi.org/10.1016/j.carbon.2013.11.038

Sgro, L. A., D'Anna, A., & Minutolo, P. (2010). Charge distribution of incipient flame-generated particles. *Aerosol Science and Technology, 44*, 651–662. https://doi.org/10.1080/02786826.2010.483701

Sgro, L. A., D'Anna, A., & Minutolo, P. (2011). Charge fraction distribution of nucleation mode particles: New insight on the particle formation mechanism. *Combustion and Flame, 158*, 1418–1425. https://doi.org/10.1016/j.combustflame.2010.11.010

Sirignano, M., Bartos, D., Conturso, M., Dunn, M., D'Anna, A., & Masri, A. R. (2017). Detection of nanostructures and soot in laminar premixed flames. *Combustion and Flame, 176*, 299–308. https://doi.org/10.1016/j.combustflame.2016.10.009

Sirignano, M., Russo, C., & Ciajolo, A. (2020). One-step synthesis of carbon nanoparticles and yellow to blue fluorescent nanocarbons in flame reactors. *Carbon N Y, 156*, 370–377. https://doi.org/10.1016/j.carbon.2019.09.068

Sobczyk, A. T., & Jaworek, A. (2021). Carbon microstructures synthesis in low temperature plasma generated by microdischarges. *Applied Sciences, 11*. https://doi.org/10.3390/app11135845

Souza, V. G. L., & Fernando, A. L. (2016). Nanoparticles in food packaging: Biodegradability and potential migration to food-A review. *Food Packaging and Shelf Life, 8*, 63–70. https://doi.org/10.1016/j.fpsl.2016.04.001

Sung, D. H., Doshi, S. M., Murray, C., Rider, A. N., & Thostenson, E. T. (2020). Electrophoretic deposition: Novel in situ film growth mechanism of carbon nanocomposite films within non-conductive fabrics for multi-scale hybrid composites. *Composites Science and Technology, 200*. https://doi.org/10.1016/j.compscitech.2020.108415

Takeuchi, M. (2006). Adhesion forces of charged particles. *Chemical Engineering Science, 61*, 2279–2289. https://doi.org/10.1016/j.ces.2004.06.051

Tassopoulos, A. O. M. J., & Rosner, E. (1989). Simulation of microstructure/mechanism relationships in particle deposition. *AIChE Journal, 35*, 967–980.

Thompson, J. E. (2018). Airborne particulate matter: Human exposure and health effects. *Journal of Occupational and Environmental Medicine, 60*, 392–423. https://doi.org/10.1097/JOM.0000000000001277

Tolmachoff, E. D., Abid, A. D., Phares, D. J., Campbell, C. S., & Wang, H. (2009). Synthesis of nano-phase TiO2 crystalline films over premixed stagnation flames. *Proceedings of the Combustion Institute, 32 II*. https://doi.org/10.1016/j.proci.2008.06.052, 1839–45.

Vemury, S., Pratsinis, S. E., & Kibbey, L. (1997). *Electrically controlled flame synthesis of nanophase TiO 2 , SiO 2 , and SnO 2 powders*.

Veronesi, S., Commodo, M., Basta, L., De Falco, G., Minutolo, P., Kateris, N., et al. (2022). Morphology and electronic properties of incipient soot by scanning tunneling microscopy and spectroscopy. *Combustion and Flame, 243*. https://doi.org/10.1016/j.combustflame.2021.111980

Vishnyakov, V. I., Kiro, S. A., Oprya, M.v., & Ennan, A. A. (2014). Coagulation of charged particles in self-organizing thermal plasmas of welding fumes. *Journal of Aerosol Science, 76*, 138–147. https://doi.org/10.1016/j.jaerosci.2014.06.010

Vitiello, G., De Falco, G., Picca, F., Commodo, M., D'Errico, G., Minutolo, P., et al. (2019). Role of radicals in carbon clustering and soot inception: A combined EPR and Raman spectroscopic study. *Combustion and Flame, 205*, 286–294. https://doi.org/10.1016/j.combustflame.2019.04.028

Volkov, E. N., Sepman, A v, Kornilov, V. N., Konnov, A. A., Shoshin, Y. S., & de Goey, L. P. H. (2009). Towards the mechanism of DC electric field effect on flat premixed flames. *Proceedings of the European Combustion Meeting*.

Wang, Y., Nathan, G. J., Alwahabi, Z. T., King, K. D., Ho, K., & Yao, Q. (2010). Effect of a uniform electric field on soot in laminar premixed ethylene/air flames. *Combustion and Flame, 157*, 1308–1315. https://doi.org/10.1016/j.combustflame.2010.03.001

Wang, M., Yao, G., Sun, Y., Yang, Y., & Deng, R. (2023). Exposure to construction dust and health impacts – a review. *Chemosphere*, 311. https://doi.org/10.1016/j.chemosphere.2022.136990

Xiao, J., Momen, R., & Liu, C. (2021). Application of carbon quantum dots in supercapacitors: A mini review. *Electrochemistry Communications*, 132. https://doi.org/10.1016/j.elecom.2021.107143

Xia, X., Zhong, Z., & Weng, G. J. (2017). Maxwell–Wagner–Sillars mechanism in the frequency dependence of electrical conductivity and dielectric permittivity of graphene-polymer nanocomposites. *Mechanics of Materials, 109*, 42–50. https://doi.org/10.1016/j.mechmat.2017.03.014

Xiong, G., Kulkarni, A., Dong, Z., Li, S., & Tse, S. D. (2017). Electric-field-assisted stagnation-swirl-flame synthesis of porous nanostructured titanium-dioxide films. *Proceedings of the Combustion Institute, 36*, 1065–1075. https://doi.org/10.1016/j.proci.2016.08.079

Yang, Y., Zhang, H., Li, C., Li, C., Yu, Z., & Yu, K. (2021). Diffusion charging of nanometer-sized liquid aerosol particles. *Journal of Physics D Applied Physics, 54*. https://doi.org/10.1088/1361-6463/abdefd

Zhang, Y., Petibone, D., Xu, Y., Mahmood, M., Karmakar, A., Casciano, D., et al. (2014). Toxicity and efficacy of carbon nanotubes and graphene: The utility of carbon-based nanoparticles in nanomedicine. *Drug metabolism reviews, 46*, 232–246. https://doi.org/10.3109/03602532.2014.883406

Zhang, S., Song, H., Guo, P., Zhou, J., & Chen, X. (2010b). Formation of carbon nanoparticles from soluble graphene oxide in an aqueous solution. *Carbon N Y, 48*, 4211–4214. https://doi.org/10.1016/j.carbon.2010.07.025

Zhang, L. L., Zhou, R., & Zhao, X. S. (2010a). Graphene-based materials as supercapacitor electrodes. *Journal of Materials Chemistry, 20*, 5983–5992. https://doi.org/10.1039/c000417k

Zhao, H., Liu, X., & Tse, S. D. (2008). Control of nanoparticle size and agglomeration through electric-field- enhanced flame synthesis. *Journal of Nanoparticle Research, 10*, 907–923. https://doi.org/10.1007/s11051-007-9330-7

Zhao, X. Y., Yang, W., Li, C., Wang, X., Lim, S. L., Qi, D., et al. (2015). Effects of Damkhöler number of evaporation on the morphology of active layer and the performance of organic heterojunction solar cells fabricated by electrospray method. *Solar Energy Materials and Solar Cells, 134*, 140–147. https://doi.org/10.1016/j.solmat.2014.11.029

Zheng, F. (2002). Thermophoresis of spherical and non-spherical particles: A review of theories and experiments. *Advances in Colloid and Interface Science, 97*, 255–278.

Zhitomirsky, I. (2006). Electrophoretic deposition of organic-inorganic nanocomposites. *Journal of Materials Science, 41*, 8186–8195. https://doi.org/10.1007/s10853-006-0994-7

Zigan, L. (2018). Overview of electric field applications in energy and process engineering. *Energies, 11*. https://doi.org/10.3390/en11061361